International Journal of Plasticity 134 (2020) 102850

Contents lists available at ScienceDirect

International Journal of Plasticity

journal homepage: http://www.elsevier.com/locate/ijplas

The effect of local chemical ordering on Frank-Read source activation in a refractory multi-principal element alloy

Lauren T.W. Smith [a,b,*], Yanqing Su [c], Shuozhi Xu [d], Abigail Hunter [b], Irene J. Beyerlein [a,c,d]

[a] Materials Department, University of California, Santa Barbara, Santa Barbara, CA, USA
[b] X Computational Physics, Los Alamos National Laboratory, Los Alamos, NM, USA
[c] Department of Mechanical Engineering, University of California, Santa Barbara, Santa Barbara, CA, USA
[d] California NanoSystems Institute, University of California, Santa Barbara, Santa Barbara, CA, USA

ARTICLE INFO

Keywords:
Dislocations
Dynamics
Inhomogeneous material
Metallic material
Medium entropy alloy

ABSTRACT

In this work, we investigate the operation of Frank-Read (FR) sources in a refractory multi-principal element alloy (MPEA). Simulations of discrete dislocation motion in MPEAs is enabled by the development of a phase field dislocation dynamics model that treats the atomic-scale fluctuations in lattice energies across the glide plane, present due to local ordering in the chemical composition within the nominally random MPEA atomic structure. We consider, through simulation, a range of length scales over which ordering occurs, varying from short-range lengths, a few times dislocation core width, to long-range lengths, an order of magnitude longer than the core. Characteristic of this body-centered cubic MPEA, the simulations also include screw/edge character dependence in glide resistance, as informed by atomic scale simulation. The critical stresses to activate the source for the same source size are found to be statistically distributed, as a direct consequence of the underlying variation in lattice energy. Analysis of critical state for activating edge and screw FR sources in the MPEA reveals that FR source operation occurs via a two-step mechanism, involving athermal kink-pair formation, unlike the conventional FR source operation in a material with no composition fluctuations. This mechanism lowers the average critical stress required to activate the FR source and causes the statistical dispersion in critical stress to depend on the range of composition ordering. More importantly, it leads to a more severe dependence of source strength on FR source length than predicted by line tension alone.

1. Introduction

Multi-principal element alloys (MPEAs), including medium and high entropy alloys and complex concentrated alloys, are materials with no single dominant element species. They instead contain frequently changing atom types on a disordered lattice. This unusual atomic structure results in atomic-scale fluctuations in chemical composition and configuration and large lattice distortions. Experiments and atomic-scale modeling have shown that the underlying mechanisms, microstructures, and properties of MPEAs are distinct from those of the pure metals that constitute their composition (Rao et al., 2017b, 2019a; Maresca and Curtin, 2020a; Miracle and

* Corresponding author.Materials Department, University of California, Santa Barbara, Santa Barbara, CA, USA.
E-mail address: Ltsmith@ucsb.edu (L.T.W. Smith).

https://doi.org/10.1016/j.ijplas.2020.102850
Received 24 July 2020; Accepted 23 August 2020
Available online 1 September 2020

Senkov, 2017). Their structural and plastic performance have been equally intriguing with some combinations displaying high yield strength, high ductility, good fatigue resistance, corrosion resistance, and thermal stability unlike their pure metal counterparts (Miracle and Senkov, 2017; Zhang et al., 2014). For example, the first and most studied of its kind, the face-centered cubic (FCC) high entropy Cantor alloy, CoCrFeNiMn, has shown superior ductility and strain hardening, but has a relatively low yield strength at room temperature (Gali and George, 2013; Otto et al., 2013). This had lead to recent work focused on designing compositions, microstructures, nanostructures, precipitation, and investigating the effects of grain size and temperature on yield strength to improve the plastic properties further (Hasan et al., 2019; Ming et al., 2019; Schneider et al., 2020; Li et al., 2019b; Brechtl et al., 2019).

Though MPEAs are defined as having a disordered structure, it has been predicted both experimentally and computationally that they actually contain some level of short-range order (Singh et al., 2015; Fernández-Caballero et al., 2017; Wróbel et al., 2015; Zhang et al., 2017). This ordering may be controlled by processing conditions and alloy composition, making it a highly tunable parameter for designing MPEAs (Ding et al., 2018). Computational models show ordering in the first few nearest neighbor shells, suggesting that the extent of short-range order is limited to a few nanometers (Fernández-Caballero et al., 2017). Recent experiments have measured short-range order for the first time and found diffuse domains on the order of 1 nm in CrCoNi, which affected properties including the stacking fault energy and the hardness (Zhang et al., 2020). However, it is still not fully understood how the degree and extent local affect complex processes such as dislocation nucleation and propagation.

While MPEAs with FCC crystal structures received much of the initial attention, over the last decade, MPEAs with body-centered cubic (BCC) crystal structures have proven to be equally fascinating. In particular, refractory MPEAs, composed of refractory elements such as Zr, Nb, Mo, Hf, Ta, and W (Couzinié and Dirras, 2018) have shown promise for high-temperature applications, due to their high yield strengths at elevated temperatures (Senkov et al., 2018). However, many refractory MPEAs exhibit low ductility at room temperature similar to pure refractory metals (Couzinié and Dirras, 2018).

Due to the BCC crystal structure and some of the trends in mechanical response, one may expect that the underlying mechanisms for plastic flow in refractory MPEAs are similar to that of pure BCC metals. In ambient conditions, the plastic behavior of BCC metals and conventional alloys is dominated by glide of screw dislocations, which move via thermally activated kink-pair nucleation (Seeger, 1956; Dezerald et al., 2015; Ji et al., 2020; Shinzato et al., 2019). Recent experimental observations of dislocations in HfNbTaTiZr reveal numerous straight screw dislocations aligned in the $\langle 111 \rangle$ direction and high levels of dislocation debris (Couzinié and Dirras, 2018; Couzinié et al., 2015; Lilensten et al., 2018), which is consistent with current knowledge of BCC metals. However, there is evidence that high concentrations of alloying elements decreases the screw/edge mobility ratio in refractory metals (Statham et al., 1972; Mompiou et al., 2018), especially at small strains (Dirras et al., 2015). Additionally, the varying chemical landscape within an MPEA may affect these mechanisms as dislocations are naturally kinked and kink-pair migration becomes the limiting step (Maresca and Curtin, 2020b; Rao et al., 2017a, 2019b). Thus, it is not yet clear how much of our current knowledge of plastic deformation in BCC metals can be applied to these complex alloy systems. Even if the mechanisms are the same, any alterations in how they operate substantially affect their overall response. In addition, there is still much unexplored composition space, especially if one considers non-equiatomic compositions, allowing for the design of new alloys with attractive properties for many applications.

These issues have broad implications on the formulations used by models and simulation techniques currently available for studying plastic deformation mechanisms and behavior. Due to their unique atomic-scale constitution, a large portion of the modeling studies investigating dislocations in MPEAs to date utilize atomistic methods, like molecular dynamics (MD) or molecular statics (MS). Atomistic models have shown that dislocations in these materials adopt wavy configurations to lower their total energy by finding favorable local environments (Rao et al., 2017a, 2019a; Maresca and Curtin, 2020a, 2020b; Chen et al., 2020a). These shape changes can increase the proportion of edge-oriented and mixed-type dislocations in a configuration that may be predominantly straight screw-type dislocations in a more homogeneous material. Also, the variation in chemical composition throughout the MPEA creates both favorable and unfavorable local environments. Because the local arrangement of constituent atoms differ along the dislocation line, the core structure is not uniform along the length of the dislocation (Rao et al., 2019a). Studies show that the stress required to move a long dislocation is enhanced relative to a pure reference case because the dislocation will have to pass through higher energy local environments as it propagates through the material, leading to inherent dislocation pinning points within the alloy (Rao et al., 2017a). In BCC metals, dislocations of screw character have a much higher Peierls barrier or stress than those with non-screw character (Weinberger et al., 2013a; Kang et al., 2012). Rao et al. (2017a) reported that, unlike in pure BCC metals, the critical resolved shear stress for an edge dislocation was only slightly lower than that for a screw dislocation in a model BCC MPEA. Recent MD work has suggested that edge dislocations play an increasing role in dictating the plastic flow of refractory MPEAs as temperatures increase (Maresca and Curtin, 2020a). Atomistic methods such as MD and MS are limited by the chosen interatomic potential, which may or may not accurately capture the behavior and core structure of dislocations in BCC metals. Since MPEAs are a relatively new class of materials and the composition space is vast, reliable potentials are only available for few MPEAs (Choi et al., 2018; Bahramyan et al., 2020; Li et al., 2019a, 2020).

Due to the limitations of atomic-scale methods, there is a need for meso- and macro-scale models that can examine deformation mechanisms that prevail at the length scales of one or more discrete dislocations, and in a manner that is time and cost effective for investigating the unexplored MPEA composition space. However, for MPEAs, such models must also be able to capture the atomic-scale fluctuations in local composition that atomistic simulations have shown play a significant role in the motion and dynamics of dislocations. The discrete dislocation dynamics (DDD) simulation method is one such mesoscale technique that has been used to study dislocation roughening due to random forces resulting from the underlying atomic-scale disorder characteristic of MPEAs (Zhai and Zaiser, 2019). Like DDD, phase-field dislocation dynamics (PFDD) is another mesoscale simulation method that can be directly informed by atomic-scale calculations and can reach the length and time scales corresponding to one or more groups of discrete

dislocations. For the FCC Cantor MPEA, for instance, variable stacking fault energies from MD were incorporated into a PFDD model (Zeng et al., 2019). They reported that the critical stress to move a single dislocation increased with the magnitude of the underlying fluctuations in the stacking fault energy. A similar conclusion was reached by Zhang et al. (2019) who employed a one-dimensional Peierls-Nabarro model to study the effect of random fluctuations in lattice energy in the BCC MPEA MoNbTaWV on the critical stresses to move a long dislocation. A very recent PFDD study, incorporating generalized stacking fault energy (GSFE) surfaces from density functional theory (DFT), probed the effect of different chemical and configurations on equilibrium dislocation core structures in an FCC medium-entropy alloy (Su et al., 2019b), showing a strong effect on the stacking fault width. Thus, these mesoscale techniques, in combination with atomic-scale calculations, are demonstrating abilities to provide useful insight into dislocation behavior.

In this work, we employ PFDD to study the mechanisms and critical stresses associated with the activation of Frank-Read (FR) dislocation sources of either screw and edge character in a refractory MPEA. FR sources are a primary mechanism of dislocation generation, and the stresses to activate them are known to greatly affect yield strength and plastic flow in metals (Frank and Read, 1950; Chen et al., 2020b; Zhu et al., 2014; Zhang and Ngan, 2018). Because the behavior of dislocations in MPEAs will be statistical in nature due to the composition fluctuations, many iterations of each simulation are required to understand the average behavior. Therefore, a mesoscale modeling technique such as PFDD is necessary to reach the required lengths, times, and number of simulations. Atomistic methods, such as MD or DFT, are limited by computational power, and therefore cannot be used to study Frank-Read sources in a statistical manner. We apply the model to an equal-molar MoNbTi MPEA, which forms a single-phase BCC structure (Senkov et al., 2019). This MPEA exhibits an attractive combination of plastic properties, with a 1100 MPa room temperature compressive yield stress and excellent thermally stability in yield stresses up to 1200°C. With atomic-scale data from MS and DFT calculations, we build a PFDD model for MoNbTi that considers both chemical composition fluctuations of varying ranges from less than 1 nm to over 10 nm and dislocation character-dependent glide resistance. We find that the critical stress to nucleate dislocations from FR sources is statistical in nature and the variability in critical stress strongly depends on the range of the composition fluctuations. Analysis of the critical configurations for activation identifies a two-step process for FR source activation that involves athermal kink-pair formation at a location in the source length where the energy barrier is low. We show that it leads, on average, to lower critical stresses in the MPEA than in the reference material without composition fluctuations. Another important consequence is a much more severe size effect of FR source length on the critical stress than that derived from line tension alone. For the first time, we show how the length scale of underlying composition variations affects the operation of a FR source and show that a distinct mechanism controls the behavior of FR sources in MPEAs as opposed to that in pure materials.

This paper is structured as follows. We first review the PFDD formulation as it applies to glide in BCC crystals. We follow with a description of the atomistic methods used to provide information on the range of lattice energies penalties associated with composition fluctuations, and screw/non-screw orientation-dependent resistance against dislocation glide that define refractory MPEAs. Next in Section 3, we describe the model for FR sources in two types of materials. The first one is a reference, homogeneous approximation of MoNbTi, without composition fluctuations, but bearing the same bulk elastic moduli and lattice constants as the nominal random solid solution of this MPEA. The second one is the actual, heterogeneous MPEA MoNbTi, which includes variations in lattice energy due to changes in the local chemical composition. In Section 4, we calculate the distribution of critical stresses required to nucleate a dislocation loop from the FR sources, with and without line orientation-dependent resistance. We follow with an analysis of the mechanisms for dislocation nucleation in the MPEA compared to the conventional ones seen in the reference material and implications of these mechanisms on the statistical dispersion and size effects on these stresses in Section 5. Finally, the main conclusions tying local composition ordering to changes in FR source operation, reductions in critical stresses, and enhanced size effects are drawn in Section 6. Although we focus our attention on one MPEA, the formulation, model, and trends described here can be generalized to consider other MPEA compositions and crystal structures.

2. Methods

2.1. Phase field dislocation dynamics (PFDD)

The PFDD model is used to simulate dislocations in the BCC lattice of MoNbTi. PFDD uses order parameters in 3D space, $\mathbf{r} = (x,y,z)$, to track the location and motion of individual dislocations (Beyerlein and Hunter, 2016). Each order parameter, $\phi_\alpha(\mathbf{r})$, is a scalar field variable that is defined for the slip system, α, with slip plane normal, $\mathbf{n}_\alpha$, and slip direction, s_α, on which that parameter tracks dislocation motion. For example, on a single slip system, a value of $\phi(\mathbf{r}) = 0$ indicates that the crystal is unslipped at $\mathbf{r}$, and when $\phi(\mathbf{r}) = 1$, a dislocation has passed point $\mathbf{r}$. Additional positive and negative integer jumps indicate subsequent slip by positive and negative dislocations, respectively. Intermediate, non-integer values correspond to the dislocation line itself. While this approach can be applied generally to many active slip systems, this work focuses on dislocation glide on the $\left(1\bar{1}0\right)$ plane with a Burgers vector in the [111] direction. Thus, only one active order parameter is required and the subscript is henceforth neglected. Because the order parameters track the motion and interaction of dislocations, which mediate plastic flow in metals, the plastic strain can be written as a function of the active order parameters :

$$\boldsymbol{\varepsilon}^{\mathrm{p}}(\varphi) = \frac{1}{2}\frac{b\varphi}{d_{110}}(\boldsymbol{s}\otimes\boldsymbol{n} + \boldsymbol{n}\otimes\boldsymbol{s}) \tag{1}$$

where is the magnitude of the Burgers vector, is the interplanar spacing between $\left(1\bar{1}0\right)$ planes, and bold variables indicate vectors.

The slip direction corresponds to the normalized Burgers vector such that $\mathbf{b} = b\mathbf{s}$. The evolution of the order parameters, and thus, the dislocations within the system, is achieved by minimizing the total energy density, ψ, of the system through the application of Ginzburg-Landau dynamics:

$$\dot{\varphi} = -m_0 \partial_{\varphi} \psi \tag{2}$$

where m_0 is the Ginzburg-Landau coefficient.

The total energy density of the system is given by the combination of three components, the elastic energy density ψ_{elas}, the lattice energy density ψ_{latt}, and the externally applied energy density ψ_{ext}, which can all be expressed in terms of the order parameters:

$$\psi(\varphi) = \psi_{elas}(\varphi) + \psi_{latt}(\varphi) - \psi_{ext}(\varphi) \tag{3}$$

The formulations of the elastic strain energy density and energy density due to externally applied stress follow the standard expression (Koslowski et al., 2002; Beyerlein and Hunter, 2016), which can be written as:

$$\psi_{\text{elas}}(\boldsymbol{\varepsilon}, \varphi) = \frac{1}{2}[\boldsymbol{\varepsilon} - \boldsymbol{\varepsilon}^{\text{p}}(\varphi)] \cdot \mathbf{C}[\boldsymbol{\varepsilon} - \boldsymbol{\varepsilon}^{\text{p}}(\varphi)] \tag{4}$$

$$\psi_{ext} = \boldsymbol{\sigma}_{\text{app}} \cdot \boldsymbol{\varepsilon}^{\text{p}}(\varphi) \tag{5}$$

where $\mathbf{C}$ is the elastic stiffness tensor, ε represents the total strain, and σ_{app} is the externally applied stress. The above equations use an additive decomposition of total strain in elastic and plastic strains. In PFDD, we work with energies relevant to discrete dislocations, one of which is the elastic strain energy produced by a discrete dislocation onto the surrounding material outside its core (Eq. (4)). We use the formulation set by continuum mechanics dislocation theory (Kröner, 1959). In doing so, we assume a continuous displacement field is generated from which we calculate a displacement gradient. The displacement gradient can be decomposed into an elastic part and plastic part. Physically, this decomposition is satisfied as the displacement from the elastic portion arises from the stretching of atomic bonds but the plastic part arises from breaking and shifting bonds but otherwise does not change bond length. A multiplicative decomposition, on the other hand, applies to the decomposition of the deformation gradient into its plastic and elastic parts rather than the displacement gradient. The deformation gradient is used in constitutive laws in which plasticity is modeled by homogeneous crystallographic slip on slip systems but not by individual dislocations represented discretely by their line and Burgers vector.

The lattice energy density, ψ_{latt}, corresponds to the Peierls barrier that a dislocation must overcome in order to glide. The functional form of this term thereby varies based on the crystal structure of the material under consideration. Formulations have been previously proposed for FCC (including high entropy alloys) (Xu et al., 2019a; Zeng et al., 2019; Su et al., 2019b), BCC (Peng et al., 2020; Xu et al., 2020c), and hexagonal closed packed (HCP) (Albrecht et al., 2020) metals. To apply generally to these three crystal structures ψ_{latt} is required to account for differences in crystallography and permit dissociation of perfect dislocations into extended dislocations, if energetically favorable. In the case of BCC metals and alloys, the dislocation cores remain compact (Ismail-Beigi and Arias, 2000; Mapar et al., 2017; El Ters and Shehadeh, 2019; Gröger and Vitek, 2020), and can, therefore, be represented at the mesoscale as a perfect dislocation. The influence of the atomic structure of dislocation core on ψ_{latt} needs to be considered indirectly in PFDD and with information from atomic-scale calculations. The Peierls potential in many pure BCC metals have a sine-squared (or sinusoidal) form (Weinberger et al., 2013b). Accordingly, ψ_{latt} is represented by:

$$\psi_{lattice}(\varphi) = A(x,y)\beta(\theta)\sin^2(\pi\varphi) \tag{6}$$

where A(x,y) corresponds to the energy barrier field in the (x,y)-plane and β(ϑ) is a function describing the dislocation orientation-dependent barrier to in-plane glide, ϑ where is the character angle. The is the angle between the Burgers vector and the dislocation line. An angle of 0° corresponds to a screw dislocation and 90° to an edge dislocation. In prior PFDD applications to pure metals (Xu et al., 2020c), A was constant. MPEAs, however, exhibit atomic-scale fluctuations in chemical composition and configuration, rendering a spatially varying A(x,y) within the slip plane. In a real MPEA, the energy barrier will vary in all 3 dimensions. However, here we are considering only individual dislocations confined to a single slip plane, so variation in the z-direction is neglected. In simulation, as a dislocation glides within its slip plane, it will encounter different local environments which correspond to varying lattice energies. Here, we elect to inform the Peierls barrier coefficients and the orientation-dependent barrier function with calculations from atomistic methods, as described next.

2.2. Informing the lattice energy with molecular statics

Atomistic simulations are used to inform the orientation-dependent resistance, β(ϑ), which incorporates the difference in mobility between edge, screw, and mixed-type dislocations in BCC metals (Peng et al., 2020). In pure metals, dislocations lines are typically not straight and the character of a dislocation varies along the line due to line curvature. In MPEAs that show wavy dislocation line configurations, the dislocation line character will vary even more drastically along the dislocation line. This may become even more pronounced as the system evolves and the dislocation line moves, curves, and bows. Thus, we utilize an on-the-fly dislocation character identification scheme (Peng et al., 2020). This procedure utilizes the gradient of the order parameter, $\vec{\nabla}\varphi$, in 3D space to determine where the dislocation line is each time step, and its direction of maximum change. Using the slip plane normal, $\mathbf{n}$, the vector tangent to the dislocation line, $\mathbf{t}$, at all points can be determined as:

$$\mathbf{t}(\mathbf{r},t) = \frac{\vec{\nabla}\varphi(\mathbf{r},t) \times \mathbf{n}}{|\vec{\nabla}\varphi(\mathbf{r},t) \times \mathbf{n}|} \tag{7}$$

where the tangent vector and gradient of the order parameter may change position over time, t, during evolution of the system. Once the tangent vector at all points along a dislocation curve, line or loop has been determined, the character angle, ϑ, can easily be identified by:

$$\theta = \arccos(\mathbf{t}(\mathbf{r},t) \cdot \mathbf{s}) \tag{8}$$

where we note that the tangent vector and slip direction are already normalized vectors.

Once the character angle of all dislocation lines within the system is known, some transition between the Peierls barrier for screw dislocations and the Peierls barrier for edge dislocation must be defined. Because screw dislocation motion dominates plastic flow in BCC metals, Peierls barriers of screw dislocations in pure BCC metals have been calculated previously with DFT (Weinberger et al., 2013b; Itakura et al., 2012; Ventelon et al., 2013; Dezerald et al., 2014). However, such DFT calculations can be time consuming, and it is common for Peierls stress calculations to be performed using MS (Kang et al., 2012; Chaussidon et al., 2006), which require interatomic potentials. Furthermore, Peierls barrier calculations are less common for edge dislocations, which are well known to move more easily through the BCC crystal lattice. Even less common are Peierls stress calculations for dislocations of mixed character. As a rare case, Kang et al. (2012) calculated the {111} plane Peierls stress in Ta for the full range of possible character angles. Such calculations proved ideal for informing the mathematical form of the orientation-dependent barrier function for PFDD simulations of anisotropic loop expansion and kink-pair motion in (Peng et al., 2020). Yet, still to this day, such simulations can be time consuming to complete for many character angles and in different materials, especially MPEAs. Furthermore, they employ an interatomic potential, for which there can be many to choose from for one metal, and which can produce different results even for the same metal (Hale et al., 2014).

Recently, the local slip resistances (LSRs) for dislocations in MoNbTi were calculated using MS (Wang et al., 2020). Because of the random nature of MPEAs, there is a distribution of LSRs for both screw and edge dislocations, with edge dislocations having lower slip resistances on average. We incorporate this difference into the PFDD model through the orientation-dependent barrier function $\beta(\vartheta)$ in Eq. (6). We define this functionas

$$\beta(\theta) = \left(1 - \frac{\sigma_{edge}}{\sigma_{screw}}\right)\cos^2\theta + \frac{\sigma_{edge}}{\sigma_{screw}}, \tag{9}$$

where σ_{edge} and σ_{screw} are the average LSR for edge and screw dislocations in MoNbTi, respectively. The function provides a smooth scaling for all dislocation character types, while preserving the ratio of Peierls barriers between edge and screw dislocations as determined by MS.

Based on MS calculations of several atomic instantiations of MoNbTi, it was found that, on average, the LSR for edge dislocations is about 22% of that of a screw dislocation (Wang et al., 2020). Accordingly, $\beta(\vartheta)$ will be 1 for screw segments and 0.22 for edge segments with the magnitude of the lattice energy defined by $A(x,y)$, as shown previously in Eq. (6). In order to characterize the role of differences in screw/edge resistance, we will, in some calculations, remove the orientation-dependent resistance, in which case $\beta(\vartheta) = 1$ for all line orientations.

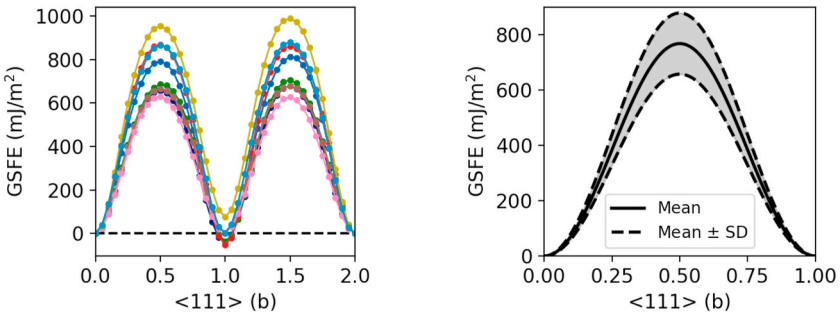

(a) DFT-calculated GSFE curves (b) GSFE curve used in PFDD

Fig. 1. The left figure shows the 24 DFT-calculated GSFE curves in MoNbTi on the {110} glide plane family. There are 12 {110}-type glide planes each with two distinct GSFE curves. The mean USFE is 768 mJ/m^2. The right shows the idealized GSFE curve used in the PFDD simulations (Eq. (6)). The peak value of the GSFE curve varies depending on local composition, so a range of peak values is shown. Because the structure used to calculate the GSFE curves requires two 1b translations in the [111] direction to return to its original configuration, there are slight differences between the starting and ending energies for each GSFE curve. The barrier height is considered to be the average between the forward and reverse barrier.

2.3. Informing the lattice energy with DFT

The lattice energy penalty, ψ_{latt}, associated with slip by a dislocation is often formulated using a GSFE curve or surface. Phase field based models have recently begun incorporating the entire GSFE surface when calculating equilibrium core structures (Xu et al., 2019b), dislocation and twin formation (Hunter and Beyerlein, 2015), and Peierls stresses for dislocations (Xu et al., 2020b) in FCC materials. For dislocations in BCC materials, however, this same class of models considered the GSFE curve along the ⟨111⟩ direction, which has a single peak barrier, called the unstable stacking fault energy (USFE) (Peng et al., 2020; Xu et al., 2020c). Advantageously, GSFE curves can be calculated readily with DFT, removing any dependence on interatomic potentials. This attribute is particularly important for MPEAs, in which the local composition and configurations vary widely on an atomic scale.

Unlike in pure metals (Su et al., 2019a), in MPEAs, GSFEs in MPEAs are area-size dependent (Xu et al., 2020a; Zhao et al., 2019), influenced by the particular composition and configuration of atoms in the plane being sheared. Here, we use GSFE curves calculated previously using DFT (Xu et al., 2020a) for {110}-type glide planes that sample a small area of the plane, representing a certain composition and configuration. These types were derived from random samplings of parallel {110}-type glide planes of small cross-sectional area taken from a nominally equi-molar MoNbTi special quasirandom structures (SQS). The corresponding USFE values from this set of GSFE curves are broadly distributed. The mean USFE is 768 mJ/m^2 and the standard deviation is 111 mJ/m^2. For comparison, the USFE calculated from DFT for pure Nb is 677 mJ/m^2, and for pure Mo it is 1443 mJ/m^2 (Xu et al., 2020c), showing that for some compositions within MoNbTi, the local USFE can be lower than that for Nb but none were higher than that for Mo. The range of USFE values for this MPEA is used to parameterize Eq. (6) to create an idealized, symmetric GSFE curve (Fig. 1b). To obtain a lattice energy density, ψ_{latt}, the USFE is divided by the interplanar spacing d_{110} to obtain the lattice energy coefficient A in Eq. (6).

2.4. Defining a reference MPEA

In order to compare the behavior of an FR source in an MPEA with that in a pure metal, we define a reference case termed *homogeneous MoNbTi* that uses the elastic constants and mean USFE (768 mJ/m^2) for MoNbTi, but with no spatial variations in the lattice energy (i.e., $A(x,y) = \mu_{usf}/d_{110}$), similar to a pure metal. The homogeneous MoNbTi also uses the same elastic moduli as the MPEA, and the same screw-edge ratio for the orientation-dependent energy barrier as defined in Eq. (9).

We also compare the MPEA with two of its pure metal constituents, Mo and Nb. The elastic constants and USFE are calculated in Xu et al. (2020c), and the screw-edge ratios are taken from the critical resolved shear stresses calculated with molecular dynamics for screw and edge dislocations (Li et al., 2020). This screw-edge mobility ratios are 30.66 and 18.11 for Nb and Mo, respectively.

2.5. Correlated spatial variation of the lattice energy

Due to fluctuations in local composition and atomic ordering, the properties of an MPEA will vary from point-to-point. This is accounted for within the PFDD model by adding a position dependence to the lattice energy in Eq. (6), which captures the differences in dislocation core energies due to the presence of differing solutes. Position-dependent lattice energy has been used previously in an FCC material using PFDD (Zeng et al., 2019), as well as in a Peierls-Nabarro model (Zhang et al., 2019). Rao et al. (2019b) showed that for nine different BCC MPEAs, the solute-dislocation interaction energy, which represents the change in dislocation energy caused by a solute atom, was strongly influenced by the change in USFE due to the solute. While solute atoms also affect dislocation energies via other means, notably the solute size and modulus misfit, the change in USFE outweighs those contributions for screw dislocations in BCC MPEAs. Therefore, varying the lattice energy in PFDD in accordance with the underlying USFE will capture the heterogeneous nature of dislocation behavior in MoNbTi. Edge dislocations may interact differently from screw dislocations with the various ensembles of atom types, and here, we account their differences through the scaling relationship in Eq. (9), which is informed by MS calculations. The formulation permits, however, alternative character-dependencies, such as one that accounts explicitly for edge versus screw dislocation interactions with specific atomic neighborhoods.

Other properties such as elastic moduli or screw-edge mobility ratio may also vary within the MPEA, but we expect these variations to be second-order compared to the variations in lattice energy. Recent calculations of an FCC MPEA revealed that the shear modulus varies within 4% of the mean for differing atomic configurations (Su et al., 2019b). Therefore, we do not expect significant variation in the elastic constants throughout the MPEA, hence the elastic stiffness tensor is assumed constant throughout the simulation cell. Calculations of the screw-edge ratio in MoNbTi show variation from 2 to 80, with a mean screw-edge ratio of 4.65 (Wang et al., 2020). However, we show in Section 5.3 that the effect of the screw-edge ratio is small compared to the effect of variations in lattice energy, so the screw-edge ratio is held constant throughout the alloy.

While an MPEA may be a nominally random solid solution, on an atomic scale, they will exhibit fluctuations in chemical composition and configuration (Fernández-Caballero et al., 2017). Since this ordering will affect how the stacking fault energies vary with position, we correlate the spatially varying lattice energy coefficient from Eq. (6) within the slip plane. Our method is based on the approach developed by Hu and Tonder (1992) for creating correlated rough surfaces. This formulation can create many independent, random surfaces quickly by using the Fast Fourier Transform, and the only inputs required are the correlation length and mean and standard deviation of the USFE distribution.

To determine a spatial varying but correlated matrix, we first define the autocorrelation function as

$$ac(x,y) = \exp\left(-\frac{2.3(x^2+y^2)^{0.5}}{l}\right) \tag{10}$$

where l is the correlation length at which the autocorrelation drops to 10%. Neighboring points spaced within are more likely to have the same USFE and when spaced beyond they are more likely to be different.

The autocorrelation matrix is then used to define a filter matrix as

$$F(x,y) = \mathcal{F}^{-1}\{\sqrt{\mathcal{F}\{ac(x,y)\}}\} \tag{11}$$

where $\mathcal{F}$ and $\mathcal{F}^{-1}$ denote the Fourier transform and its inverse, respectively. To generate a correlated matrix, an initial uncorrelated matrix, $\boldsymbol{A}_{uncorr}$, of the desired dimension is created by drawing each value from a normal distribution with mean 0 and variance 1. This uncorrelated matrix and the filter matrix are convoluted to determine the correlated matrix:

$$A_{corr}(x,y) = F(x,y) * A_{uncorr} \tag{12}$$

Finally, the correlated matrix is scaled and shifted to give the correct mean and standard deviation for A(x,y).

$$A(x,y) = \frac{s_{usf}}{d_{110}} A_{corr}(x,y) + \frac{\mu_{usf}}{d_{110}} \tag{13}$$

where μ_{usf} and s_{usf} are the mean and standard deviation of the USFE for the MPEA, calculated with DFT. While not directly apparent in Eq. (13), we note that an important parameter associated with the calculation of A(x,y) is the correlation length, l. Additional, independent surfaces are created by changing the initial matrix $\boldsymbol{A}_{uncorr}$. As long as the initial matrices are chosen randomly and are independent of one another, the final correlated matrices will also be independent.

In our simulations, eight different correlation lengths are studied: $1w_0$, $2w_0$, $3w_0$, $4w_0$, $5w_0$, $10w_0$, $15w_0$, and $20w_0$, where w_0 is the core width of a screw dislocation in homogeneous MoNbTi. The width was determined by modeling a screw dislocation under zero stress. The dislocation core is considered to be where ϕ is between 0.1 and 0.9, giving a core width of approximately 2.15b . This measured core width is highly dependent on the cutoff used to define the core. For example, using a cutoff of ϕ between 0.2 and 0.8 gives a width of 0.78b, while a cutoff of ϕ between 0.05 and 0.095 gives a width of 5.36b. We choose to use to 2.15b value as this width contains 80% of the Burgers vector associated with the dislocation, but caution should be exercised when interpreting this value as an absolute measurement of dislocation core width. As the extent of short-range order is expected to be on the order of nanometers, we choose a range of correlation lengths that span from about 0.5 nm to more than 10 nm. The exact value of the correlation length in a MoNbTi sample will depend on external factors such as temperature and processing conditions. Fig. 2 shows example $\{1\bar{1}0\}$ surfaces for six correlation lengths. For the sake of presentation, we color the regions of like composition with their local peak value of A. While the correlation length in each glide surface is fixed, the range of composition ordering are still distributed across the plane and transitions between regions of like composition are smooth.

3. Model set up

Fig. 3 presents a schematic of the FR source simulation set-up used in this work. We employ a cuboidal simulation cell, that is rotated such that the $[1\bar{1}0]$ slip plane normal is parallel with the z-axis. A 128x128x128 computational grid is used with an interplanar

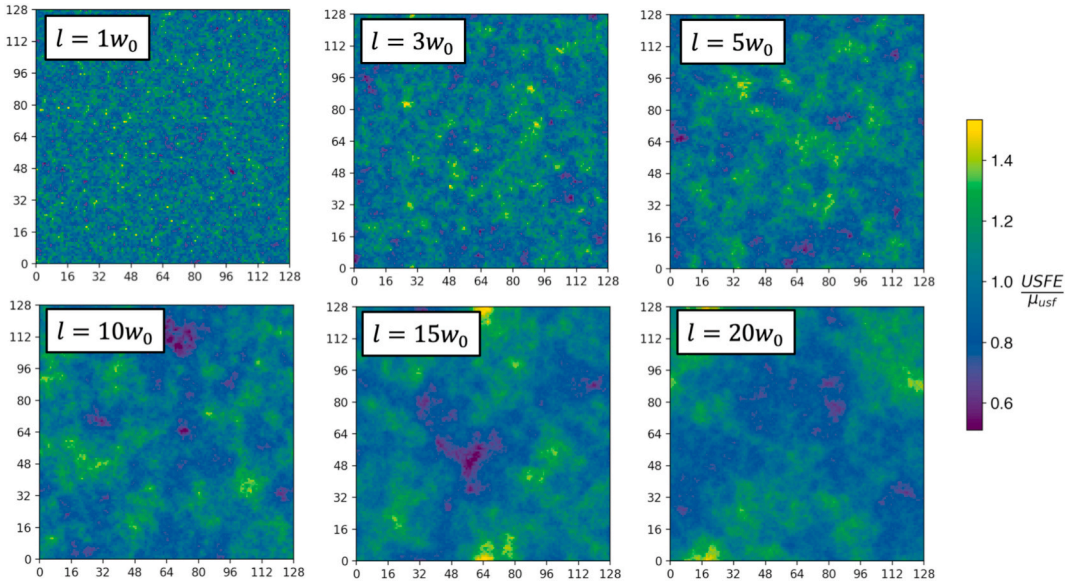

Fig. 2. Example correlated surfaces with various correlation lengths, .

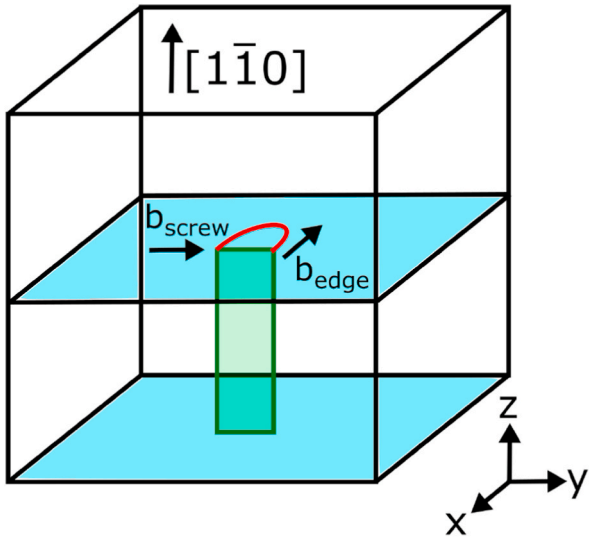

Fig. 3. The simulation setup for a Frank-Read source. A prismatic loop is shown on green. Under an applied load, a dislocation loop, shown in red, bows out from the edges of the loop on the slip planes in the center of the cell. The Frank-Read source is screw or edge-oriented depending on the orientation of the Burgers vector. (For interpretation of the references to color in this figure legend, the reader is referred to the Web version of this article.)

spacing of 0.8165b (i.e., in the z-direction) and an in-plane grid spacing of b = 2.79 Å. Calculation of the elastic strain energy, Eq. (4), utilizes a Fast Fourier Transform, and accordingly, the model employs periodic boundary conditions. Elastic anisotropy is fully accounted for within the model (Xu et al., 2019c). Elastic constants for MoNbTi were calculated using DFT and a model SQS of a 3D random solid solution of MoNbTi. The same SQS used to calculate these constants is used to calculate the lattice energies (Xu et al., 2020a). The calculations provide cubic anisotropics constants C_{11}, C_{12}, and C_{44} equal to 252.13 GPa, 134.11 GPa, and 34.41 GPa, respectively, using the energy-strain method (Su et al., 2020). For convenience, we will report critical stresses in units of the equivalent isotropic shear modulus, which, for this cubic elastic material, is 41.29 GPa.

An FR source is built in a similar fashion to phase field model set-ups used previously (Xu et al., 2020c). An FR source is created in the system by creating a prismatic loop that spans between two slip planes as shown in Fig. 3. We consider two slip systems in our simulations. The first slip system is a $(1\bar{1}0)$ slip plane with a normal in the z-direction, while the second is a slip plane perpendicular to the first with a normal in the x-direction. Both use a [111] type Burgers vectors, with the direction of the Burgers vector depending on the orientation of the FR source. To create the prismatic loop, the order parameter corresponding to the second slip system is initialized with a value of 1 on three planes: two $(1\bar{1}0)$ glide planes located at the top and bottom of the prismatic loop (indicated in blue in Fig. 3), and the plane on which the prismatic loop itself is defined (indicated in green in Fig. 3), which is normal to the $(1\bar{1}0)$ plane. This configuration results in two pinned dislocation points with non-zero order parameter values on the two glide planes. The order parameters are set to zero outside of the prismatic loop. This prismatic loop is not permitted to evolve, according to Eq. (2), and hence, it remains stationary through-out the simulations. In addition, the dislocation segment at the bottom of the prismatic loop (i.e., at z = 0) is also restricted from evolving. Only the order parameters in the slip plane at can evolve, so that the FR source can operate in this plane.

An FR source of length 20b is used in all simulations, unless stated otherwise. FR sources are studied for both edge- and screw-oriented sources with the Burgers vector oriented parallel to the FR-source for a screw-oriented source and normal for an edge-oriented, as shown in Fig. 3. To activate the source, a shear stress is applied in the direction of the Burgers vector of the initial FR source segment. The shear stress is increased in increments of 0.001μ. A timestep of 0.35 was used, and the value m_0 of in Eq. (2) was set to 1. Note that all energy densities are normalized by the shear modulus μ and the timestep and mobility constant are unitless. Following each stress increment, the system is held at the current stress state for either 3000 timesteps or until the system converges, whichever comes first. System convergence is achieved when the norm of the order parameter changes by less than 10^{-5} between successive timesteps. The critical stress is surpassed when the FR source creates a full dislocation loop. The critical stress is then defined as the mean of the previous subcritical shear stress and the current supercritical shear stress.

To ensure that a 128x128x128 simulation grid is adequate for a 20b FR source and not strongly influenced by image effects, the critical stress for a 20b screw-oriented source in the homogeneous MoNbTi reference material is calculated using simulation grids with side lengths 64, 128, and 256. The same grid resolution is used for all computational grids, which is b within the slip plane and 0.8165b in the direction normal to the slip plane (same resolution as mentioned above). The critical stress for all three sizes is 0.0885μ, indicating that the 128x128x128 grid size is adequate. As further confirmation, we note that a similar conclusion was reached in recent PFDD work on FR source operation for six BCC refractory metals, varying widely in their lattice constants and elastic moduli (Xu et al., 2020c).

4. Results

Loop expansion and the corresponding critical stresses for the FR sources are calculated for both the homogeneous MPEA, with uniform properties, and the heterogeneous MPEA, in which spatial variation in the lattice energy is considered. The critical stresses are calculated both without and with the orientation-dependent barrier function for screw-oriented sources and only with the orientation-dependence for the edge sources. To garner adequate statistics for analysis, for each l, 60 different correlated surfaces are created and FR source behavior on these surfaces is studied.

4.1. Homogeneous MoNbTi

To establish a basis for comparison, we first study the behavior of an FR source in the ideally homogeneous MPEA. Fig. 4 shows snapshots taken over time of a dislocation loop expanding from a screw-oriented FR source without and with the orientation-dependent barrier function (Fig. 4(a) and (b), respectively), and an edge-oriented FR source with the orientation-dependent barrier function (Fig. 4c) in homogeneous MoNbTi. Loop expansion is shown at the respective critical stresses for each case. These critical stress values are reported for each case in Table 1. The loop expansion over time is visualized by drawing a contour line where $\phi = 0.5$, which corresponds to the center of the dislocation core. A darker red contour line corresponds to an earlier simulation time.

In all cases, an arc bows out from the FR source, eventually expanding and breaking away as a dislocation loop, which then propagates out of the simulation cell to annihilate with its periodic images. In a screw-oriented FR source without the orientation-dependent barrier function (Fig. 4c), the dislocation loop grows more or less isotropically because the edge and screw segments have similar energetic barriers for motion. However, the loop structure is not circular because the dislocation line will attempt to maximize screw-type segments due to their lower line energy with respect to edge-type segments. When the orientation-dependent barrier is included, as in Fig. 4b and 4c, the edge segments of the dislocation move much more quickly than the screw segments, leading to the formation of an oblong dislocation loop with long screw segments. The operation of FR sources seen in these three cases can be expected and thus, it serves as a good reference to identify any potential unexpected behavior that could emerge in the MPEA.

Table 1 shows that even without the orientation-dependent barrier, the required stress to bow out a dislocation loop is higher in the screw-oriented source than the edge-oriented source. This difference arises from the higher line energy associated with edge segments than screw segments, which makes it more difficult to create an initial bow-out that introduces edge-oriented segments than one that introduces screw-oriented ones. When the orientation dependence is included in the calculations, the critical stress drops by 25% and 50% in the screw- and edge-oriented cases, respectively. While the orientation-dependent barrier does not affect the lattice energy barrier for screw segments, any orientation of the FR source requires screw, edge, and mixed-type segments be created in order to generate a complete loop, so both orientations see a drop in critical stress.

4.2. Dislocation loop waviness

With the reference behavior established, we proceed to examine the behavior of the same FR sources in the heterogeneous MoNbTi with glide planes bearing varying, correlated lattice energies. As mentioned, these landscapes are characterized by over which the barriers are similar (Fig. 2). We choose to study a wide range of because the length scale over which the USFE and/or the Peierls barrier varies in actual MPEAs is unknown but finite, and could be influenced by complex factors, such as thermodynamically driven short-range order or proximity to grain boundaries (Fernández-Caballero et al., 2017; Li et al., 2019a). For each considered, a total of 60 distinct realizations were studied for the screw- and edge-oriented cases with the orientation-dependent barrier, as well as the screw-oriented case without the orientation dependence.

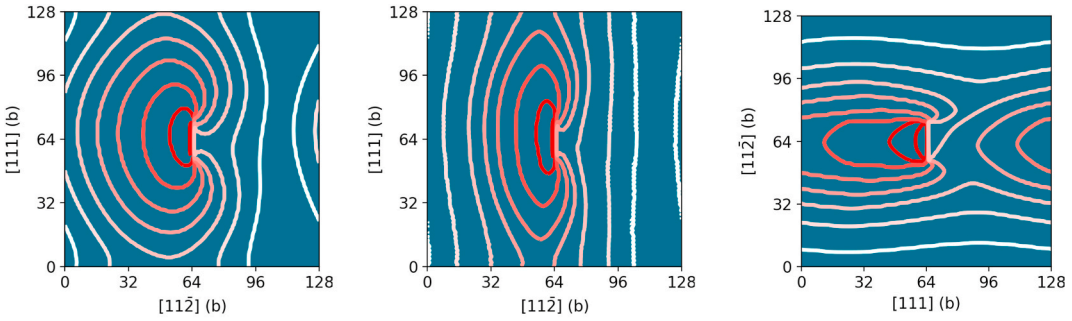

(a) Screw, $\beta = 1$ (b) Screw, $\beta = f(\theta)$ (c) Edge, $\beta = f(\theta)$

Fig. 4. Snapshots of Frank-Read source loop expansion in homogeneous MoNbTi for three source setups at their respective critical stresses. Each curve shows the dislocation at a separate timestep of the same simulation, with progressively lighter pink curves showing later timesteps. The dislocation position is estimated by drawing a contour line where $\phi = 0.5$, which corresponds to the center of the dislocation core. When $\beta = f(\vartheta)$, the orientation-dependent barrier is used and the relative barrier for motion of edge, screw, and mixed-typed dislocations differs. (For interpretation of the references to color in this figure legend, the reader is referred to the Web version of this article.)

Table 1
The critical stress for Frank-Read source activation in homogeneous MoNbTi. The critical stress is lower for edge-oriented sources than screw-oriented sources. When $\beta = f(\vartheta)$, the orientation-dependent barrier function is used and the character dependence of the lattice energy is accounted for.

Critical Stress (μ)		
	$\beta = 1$	$v = \beta = f(\vartheta)$
Screw	0.0885	0.0665
Edge	0.0705	0.0355

Fig. 5 shows the progression of dislocation loop formation and expansion from a screw-oriented FR source without and with orientation-dependent barriers and an edge-oriented source with orientation-dependent barriers for an example lattice energy surface with $l = 5w_0$. The series of dislocation lines are shown on a glide plane with spatially varying and correlated lattice energy surface. As before, they are colored to represent the variation in the peak barrier due to local chemical clustering within the MPEA encountered by the dislocation loop as it expands.

Without considering orientation-dependent barriers (Fig. 5a), loop expansion looks qualitatively similar to that of the homogeneous MoNbTi reference case in Fig. 4a, except the dislocation loop that is wavy and does not expand uniformly. As it extends and bows out under stress, the dislocation extends further through regions of low lattice energy (shown in purple), while it becomes temporarily pinned at areas of high lattice energy (shown in yellow). These high energy regions are soft obstacles, and the dislocation is able to pass through them with minimal bowing.

When the dislocation orientation dependence is taken into account (Fig. 5(b) and (c)), the growing dislocation loop from both the screw- and edge-oriented FR sources assume a much more oblong shape, as the edge segments extend much further than the screw segments owing to their lower barrier. The loops are less wavy and smoother than when the orientation-dependent barrier was not considered. In the case of the screw-oriented FR source, the dislocation grows outwards from the sides of the FR source, while the screw portions bow out slowly. Eventually the edge segments annihilate one another, permitting the two long screw segments to continue gliding away from the FR source. These two screw segments are highly curved and wavy as they navigate the varying lattice energies in the MPEA. In the edge-oriented FR source case, the edge segment grows quickly away from the source, and the two initially straight screw segments begin to bow out, eventually meeting and annihilating, releasing the loop.

In Fig. 6, we examine the effect of l on the operation of an FR source. For this analysis, we focus on the screw-oriented source without the orientation-dependent barrier function. Sample surfaces with l equal to $1w_0$ and $20w_0$ are presented. The loop on the $1w_0$ surface resembles the homogeneous case very closely (Fig. 4a), although the loop that is produced exhibits a minimal amplitude of waviness. On the other hand, the loop on the $20w_0$ surface expands unevenly, moving quickly through valleys of low lattice energy and expanding much more slowly over peaks of high energy. The behavior of FR sources in the MPEA with intermediate scale falls between these two extremes. In general, a longer range of composition ordering corresponds to greater deviations from the homogeneous case and an increase in the amplitude of the waviness in the dislocation loops that are produced.

4.3. Critical FR source activation stress

The critical stress to generate a dislocation loop from the FR source was calculated for each of the cases studied. This threshold stress is the stress required to expand the initially straight FR segment into a critical bow out configuration. The length scale over which the critical state is reached remains on the order of the FR source length itself, i.e., long before the loops shown in Figs. 5 and 6 are produced. Thus, the critical stress is established locally by the environment near the FR source. After it is reached, the loop propagates away from the source with no further increase in stress. The new loop is able to continue to glide unhindered out of the simulation cell

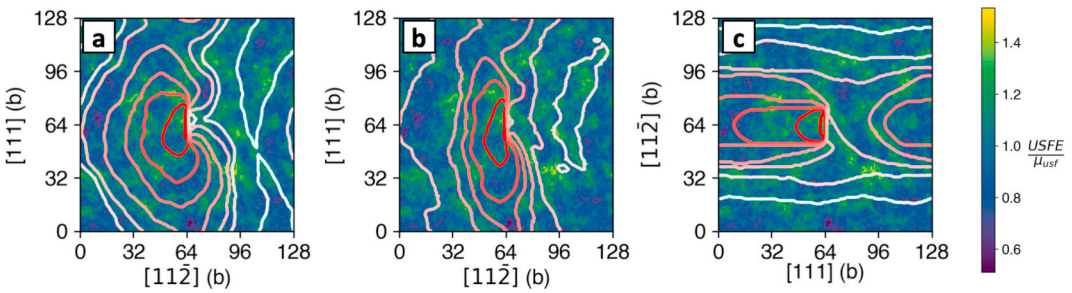

Fig. 5. The expansion of Frank-Read sources under different conditions for the same lattice energy surface with under their respective critical stresses. (a) shows a screw-oriented source without the orientation-dependent resistance, while (b) shows the same source with the use of the orientation-dependent resistance. (c) shows an edge oriented source with the orientation-dependent resistance. The red curve is drawn at the contour where $\phi = 0.5$. Several snapshots throughout the loop expansion are superimposed with the lighter colored lines corresponding to later timesteps. (For interpretation of the references to color in this figure legend, the reader is referred to the Web version of this article.)

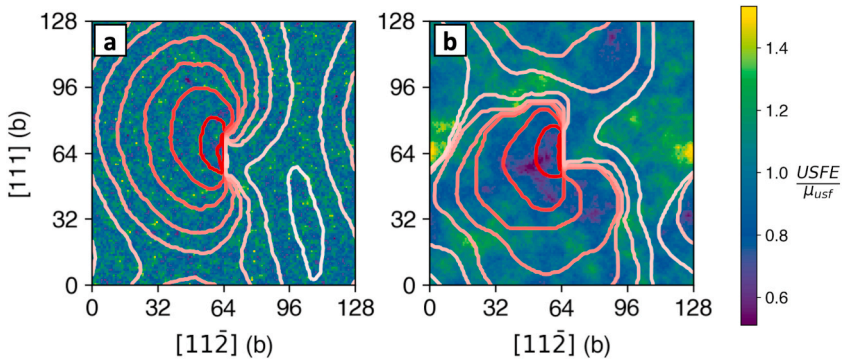

Fig. 6. The expansion of a screw-oriented Frank-Read source using surfaces with different correlation lengths: and for (a) and (b), respectively. The red curve is drawn at the contour where = 0.5. Several snapshots throughout the loop expansion are superimposed with the lighter colored lines corresponding to later timesteps. (For interpretation of the references to color in this figure legend, the reader is referred to the Web version of this article.)

and annihilate with the periodic image. This response is expected of a pure metal and seen in the case of the homogeneous material. Yet still, for the heterogeneous MPEA, the critical stress to activate the source was also sufficient to propagate the shear loop away from the source, for all FR source orientations and all realizations of all l studied. Therefore, we find that in spite of the broad range of barriers the dislocation encounters after being emitted from the source, none of them are so high that the stress required to nucleate the dislocation cannot overcome them. This response indicates that the nucleation stress is always higher than the propagation stress for the loop. Thus, overcoming line tension stills plays a dominant role in source activation.

The distributions of critical stresses at each correlation length are shown in Fig. 7 for screw-oriented sources with and without the character-dependent barrier. For comparison, the critical stresses for sources in pure Mo, pure Nb, and homogeneous MoNbTi are also plotted. When the character-dependent barrier is included, nearly all realizations of FR sources in the MPEA exceed the critical stress for Nb, and many exceed the critical stress for homogeneous MoNbTi. For both scenarios shown, the distribution of critical stresses widens as the correlation length increases. We note that prior experimental studies on a various BCC MPEAs have reported room temperature yield strengths higher than any of the constituent yield strengths. The PFDD model predicts athermal dislocation nucleation stresses for MoNbTi above that of Nb but below that of Mo since the DFT-calculated USFE values lie in between those of Nb and Mo. Studies of propagation of long dislocations and dislocations arrays and considerations of thermal effects within the model may provide a different relationship between the MPEA and its constituents.

The calculations here show that the statistical dispersion in critical stresses among the different realizations is substantial, too great in some cases to be appropriately evaluated by standard Gaussian (or normal) statistical analyses. To determine the form of their statistical distribution, the 60 calculated critical stresses at each l are fit to a variety of probability distributions, using the appropriate axes scaling.

Fig. 8 shows lognormal probability plots for the critical stress distributions at $l = 1$, 3, 5, and $20w_0$, wherein the axes are scaled such that a true lognormal distribution would manifest as a straight line. The wrong distribution would exhibit deviations from linearity, particularly at the tails. Interestingly in all cases, the lognormal distribution consistently provides the best representation, with a

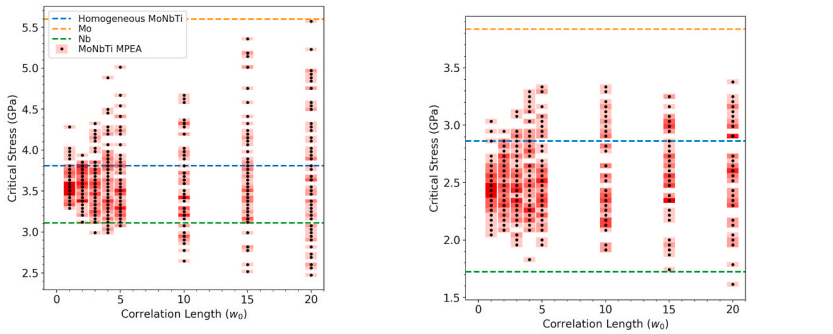

(a) Screw-Oriented Source, without Character-Dependent Barrier

(b) Screw-Oriented Source, with Character-Dependent Barrier

Fig. 7. The critical FR activation stresses for screw-oriented sources both (a) without the character-dependent barrier and (b) with the character-dependent barrier. Each black dot is a separate PFDD simulation, and the pink box represents the upper and lower bounds of the calculated critical stress. Darker pink areas represent where several realizations have the same critical stress. The dashed lines show the pure reference cases of Mo, Nb, and homogeneous MoNbTi. (For interpretation of the references to color in this figure legend, the reader is referred to the Web version of this article.)

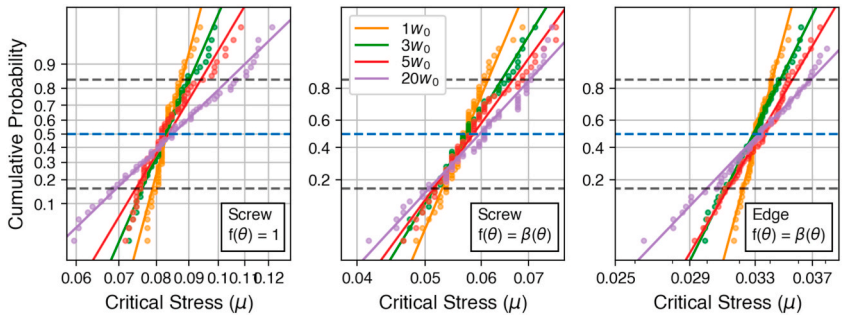

Fig. 8. Lognormal probability plots of the critical stress for Frank-Read source activation. From left to right, the plots show a screw-oriented source without the orientation-dependent resistance, a screw-oriented source with the orientation-dependent resistance, and edge-oriented source with the orientation-dependent resistance. Four correlation lengths ranging from 1 to 20w_0 are chosen to be representative. Where the best fit line crosses the dashed blue line corresponds to the mean critical stress, and the dashed black lines correspond to the mean critical stress plus or minus one standard deviation. (For interpretation of the references to color in this figure legend, the reader is referred to the Web version of this article.)

higher value than either normal or Weibull distributions. Although not shown, all other cases studied here also exhibit lognormal character. This finding implies that conventional normal estimates of the mean and dispersion would not appropriately represent the expected values and dispersion in critical stress. Further, the fact that the distributions do not follow a Weibull distribution indicates that FR source activation is not a weakest-link phenomenon. In other words, activation is not based solely on the weakest energetic barrier on which the FR source lies but on a combination of factors.

To examine altogether the effects of l, FR source orientation, and orientation-dependent resistance, Fig. 9a plots the change in the lognormal mean critical stress (dots) and standard deviation (error bars) with increasing l. For comparison, the critical stress for the equivalent homogeneous case is shown by the dashed line, which is a deterministic value. For all l and FR source characters, the mean critical stress is less than the critical stress for the homogeneous case. Evidently, introducing spatial variation in energy barriers above and below the average barriers more often weakens rather than strengthens the source. Even more importantly, we find that greater range of local chemical clustering by increasing the does not appreciably alter the mean critical stress. The critical stress remains, on average, weaker than the homogeneous material for short and long l alike.

For the screw-oriented FR sources, the effect of the dislocation orientation-dependent resistance was examined. Similar to the homogeneous MoNbTi case (Table 1), we find that considering orientation-dependent barriers decreases the critical stress to activate the source. Significantly, the reduction in critical stress relative to that for the homogeneous material is, however, the same, whether or not orientation-dependent barriers are considered. Apparently, accounting for less glide resistance for the non-screw segments is not responsible for weakening the MPEA relative to its homogeneous counterpart. Again, we find that even with screw/non-screw orientation dependence, the introduction of spatially varying barriers lowers the average critical stress compared to the same material without such dispersion.

While the range of composition ordering l has little influence on the mean critical stress, it can greatly affect the variance in the critical stresses. We calculate the coefficient of variation (COV), defined as the ratio of the standard deviation to the mean, for each lognormal distribution of critical stresses. For all FR sources, statistical variation increases as l increases. Accounting for differences in glide resistance due to dislocation orientation reduces the variation in critical stress values, particularly for larger l (5w_0 and greater),

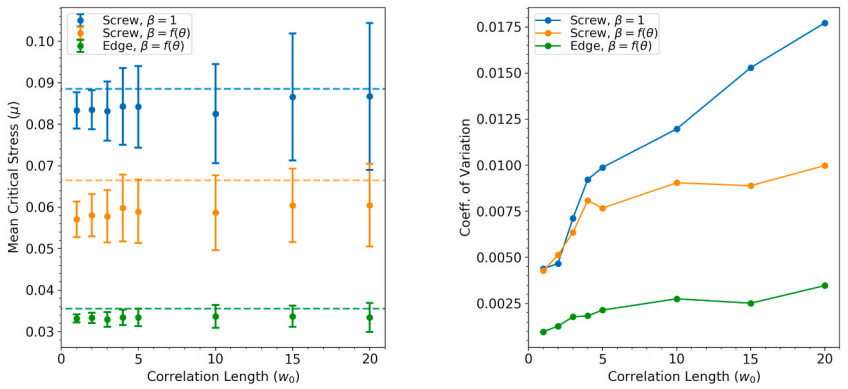

(a) Mean Critical Stress (b) Coefficient of Variation

Fig. 9. (a) The critical stresses for Frank-Read activation at each for three cases: screw without the orientation-dependent resistance, screw with the orientation-dependent resistance, and edge with the orientation-dependent resistance. In (a), the error bars represent the standard deviation of the critical stresses at each l. (b) The coefficient of variation (COV) for all three cases as a function of l.

where the variation was the greatest. Compared to the screw-oriented sources, the edge-oriented FR sources show considerably less variation in critical stress. There is only a slight increase in variation in critical stress with l.

Of particular interest is the effect of local chemical ordering on the ratio of critical stress for the screw-oriented FR source to the edge-oriented FR source. Like the homogeneous material, for the MPEA, the critical stresses for the screw-oriented sources are higher than those for the edge-oriented sources. The screw/edge ratio for the critical stresses in the homogeneous material is 1.87, which is comparable to the mean screw-edge ratio in the MPEA of 1.76. However, the composition fluctuations lead to some considerable differences in their behavior. The screw FR sources exhibit far more variation in their strength than the edge. For the edge sources, the dispersion is smaller and less sensitive to l. Also, while both screw- and edge-oriented sources are weakened relative to the homogeneous MoNbTi, the screw sources experience a more substantial drops in critical stress. The edge sources have a critical stress 6% lower than the homogeneous case, whereas screw sources have critical stresses 12% lower. Another interesting aspect is that the screw sources are always stronger than the edge sources. Even for the larger correlation lengths, $l > 5w_0$, for which the variance in critical stresses tends to be higher, the screw/edge ratio in activation stresses still remains greater than one. For any individual realization, however, the screw/edge ratio can vary substantially. In some planes, it can be as small as 1.2, whereas in other planes, the ratio exceeds 2.5.

5. Discussion

5.1. Frank-Read source activation mechanisms

In this work, we reveal significant effects of local chemical clustering on the operation of FR sources in an MPEA. The calculations show that on average the FR sources are easier to activate than the same source in a homogeneous material with nominal MPEA properties. The dispersion in the critical stresses exhibits a strong sensitivity to the range of composition ordering l. Specifically, the variance critical stress can be small when is l small but substantial when it is large, particularly when l is 4–5 times the dislocation core width. The edge-oriented FR sources also experience a reduction in strength, although less substantial than that of the screw sources. The edge sources also show smaller statistical variation in critical stress and lower sensitivity to the extent of clustering (i.e., l).

To understand the origin of these differences, we examined the incipient stages of loop production. The critical stress is associated with expansion of the initially straight dislocation segment to a certain critical configuration that must be reached in order for the loop to expand unstably. The marked differences in screw and edge source behavior suggests that different mechanisms leading to FR source activation may be involved. The FR sources in the homogeneous MoNbTi reference material operate in the classical manner with essentially no loop bowing observed at stresses below the critical stress, but once the critical stress is exceeded, the loop begins to bow out uniformly from FR source (Fig. 4).

In the heterogeneous MPEA, on the other hand, the mechanisms are different than the conventional process and depend on the line orientation of the source. When the stress is first applied to the edge-oriented sources, the line segment bows out as in the conventional case. While still at stresses below the critical stress, the edge segment glides forward, producing two long straight screw segments on either side, a consequence of its lower barrier compared to that of the screw. At the critical stress, in one of the low energy barrier regions along the screw portions, a kink-pair forms. This kink-pair expands outward initiating the formation the full dislocation loop (Fig. 10). The process of activation of the FR edge source, therefore, involves two steps: first, oblong bow-out forming long screw segments, and second, kink-pair formation on the screw segments. This basic edge-FR source process manifests in all slip plane realizations. The second step distinguishes the MPEA FR operation from that occurring in the homogeneous material.

For the screw-oriented sources in the MPEA, the dislocation loops also expands non-uniformly under stress but by a different two-step mechanism than the edge-oriented FR sources. After the stress is applied, the dislocation will first bow out in the form of a kink-pair into a small region with low lattice energy (Figs. 11 and 12). Unlike conventional kink-pairs, this kink-pair is athermal and its width is related to the extent of the low energy barrier region along the source length. Next, the edge segments of the kink-pair moves sideways. For some cases, the edge segments can glide without any further increase in stress, and the critical stress corresponds to that needed for form the first kink-pair. In other cases, sub-critical kink-pairs form, below the critical stress. The critical stress corresponds

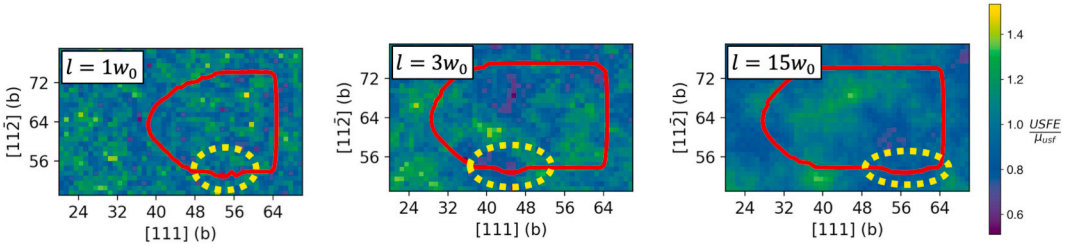

Fig. 10. The early stages of loop growth in edge-oriented Frank-Read sources with the orientation-dependent resistance. Below the critical stress, a large bow-out with straight screw segments on the sides is present. At the critical stress, a small section of one of the screw segments expands into a low energy region (highlighted by the yellow dashed circle), leading to nucleation of a kink-pair and expansion of the full dislocation loop. Examples on three surfaces with different l are shown. (For interpretation of the references to color in this figure legend, the reader is referred to the Web version of this article.)

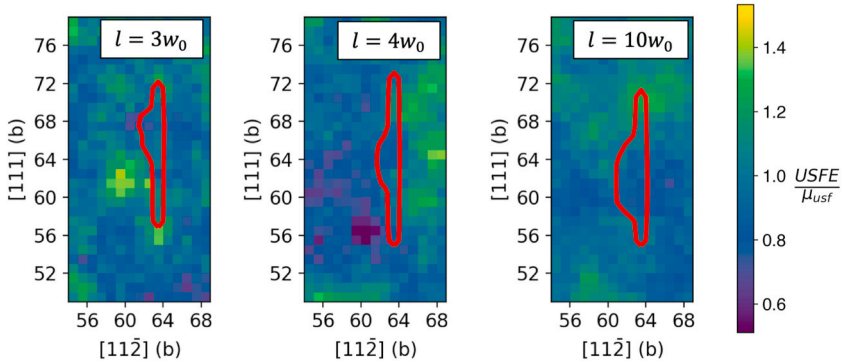

Fig. 11. The early stages of loop growth in screw-oriented Frank-Read sources without the orientation-dependent resistance. A small section of the dislocation expands into a low energy region where a kink-pair is nucleated, thus expanding the loop. Examples on three surfaces with different l are shown.

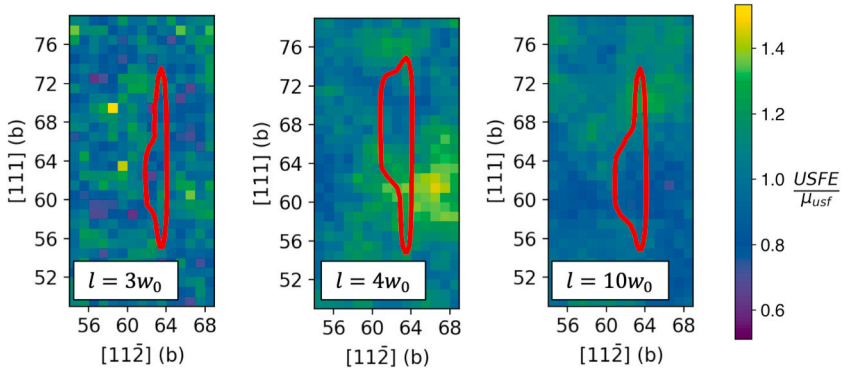

Fig. 12. The early stages of loop growth in screw-oriented Frank-Read sources with the orientation-dependent resistance. A small section of the dislocation expands into a low energy region where a kink-pair is nucleated, thus expanding the loop. Examples on three surfaces with different l are shown.

to stress needed to enable the newly formed edge segments to glide through the higher energy regions. Both steps in activating the screw-oriented source are affected by the variable energetic barriers in the glide plane, making it distinct from the operation of the same source in the homogeneous material.

This mechanism explains the reduction in the critical stress needed to operate an FR source observed when the orientation-dependent barrier is incorporated. Analysis of source operation both with and without the orientation dependence finds that this two-step mechanism for activation of screw FR sources applies even when the orientation-dependent barrier is not considered in the calculations. In all situations, source activation relies on the side edge segments of the first kink-pair to overcome the local energetic barriers. However, when dislocation motion becomes dislocation character-dependent the critical stresses are reduced even further as it becomes easier for the newly created edge and mixed type dislocations segments to move. It is expected that the larger the difference between the barriers to move screw and edge, the lower the critical stresses to activate the FR sources.

These FR source activation mechanisms can also explain many of the observed trends in the critical stress for the MPEA. Due to the varying lattice energy surface, there is likely to be a lower-than-average lattice energy region along the length of the FR source, allowing for the dislocation to bow out at a lower stress than the equivalent homogeneous material. Consequently, the FR sources on average are easier to activate in the MPEA with variable energetic barriers than the homogeneous crystal with an average barrier. Furthermore, because all of the lattice energy surfaces use the same mean and variance in the USFE, these low energy regions are equally likely to exist for all l, so the mean critical stress is not influenced by l. However, l affects the width of the peaks and valleys in lattice energy. An FR source in a material with a longer l will experience fewer variations in energy barriers along its length than one with a shorter l. Results show that the critical stress will be sensitive to the number of distinct energy barriers spanned by the FR source length. The fewer barriers encompassed by a source, the greater the variation will be among sources located in different locations of the glide plane and crystal. Particularly for $l > 8w_0$, the chances are higher that this 20b FR source will lie entirely in a region of uniform lattice energy. The influence of l on source activation for the screw-oriented sources is applicable with or without the orientation-dependent barrier. Thus, the growing dispersion in critical stress with l, i.e., extent of chemical ordering, is the same regardless of how much glide resistances differ based on dislocation orientation.

5.2. Frank-Read source size effects

The dependency of kink-pair formation on the extent of local chemical ordering suggests that many of the effects revealed here will become even more pronounced for longer FR sources. Calculations for the critical stresses for screw-oriented FR sources were repeated for source lengths that were two and three times longer (L = 40b and 60b) than the original 20b source. These simulations were performed for the screw-oriented FR source using the orientation-dependent barrier. It was determined that the current 128x128x128 cell size is sufficient for even these larger sources through a similar method as described in Section 3. The critical stresses were calculated for the same 60 energy surfaces at all eight l previously studied ranges . Statistical analysis of their distributions finds that like the 20b source, the critical stresses at each l follows a lognormal distribution.

Fig. 13a shows the mean and standard deviation in the critical stresses for each source size as a function of l. For comparison, the 20b results are also included, as well as the critical stresses for FR sources in the homogeneous material. Similar to the 20b source, the (lognormal) mean critical stresses for the larger sources do not differ appreciably with l, and the mean critical stress is always below the critical stress for the homogeneous case. As expected, the sources become easier to activate, as the source size L lengthens. The important difference, however, is the greater size effect in critical stress for the MPEA compared to the critical stress for the homogeneous material. In fact, the critical stresses for the larger sources in the MPEA drop even further below the homogeneous case than those for the 20b source. The critical stresses for the 20b source are an average of 89% of the homogeneous critical stress, whereas the critical stresses are 85% and 77% of the homogeneous case for the 40 and 60 sources, respectively. Also like the shorter 20b source, the variances in critical stresses increase as l increases.

For the homogeneous case, the FR source size effect is a consequence of overcoming line tension to reach the critical configurations leading to an approximately proportional relationship with log(L)/L (Foreman, 1967). For the FR source in the MPEA, we have shown that the mechanism for source activation is different and further, we find that it gives rise to the more severe size effect than line tension alone. Fig. 14 shows the critical configurations for the 40b and 60b FR sources. Activation requires first forming a kink-pair followed by sideways glide of the newly created edge segments. This first kink forms where the lowest energy barrier exists. By increasing the length of the source, chances of encountering a low energy barrier to form the kink-pair increases.

To compare the source size scaling effects, the critical stress for the homogeneous material was calculated for L = 24b, 30b, 36b, and 50b in addition to the previously calculated 20, 40, and 60 sources. These seven data points fit a power-law scaling very well with $R^2 = 0.986$ and give a scaling exponent of 0.11. Comparatively, the mean critical stresses for the 20b, 40b, and 60b sources in the MPEA fit a power-law scaling with a scaling exponent of 0.25. This emphasizes that the MPEA has a stronger FR source size dependence than the homogeneous reference case due to the increased presence of low energy barriers along the FR source length.

Unlike the conventional FR source operation, the FR source behavior in an MPEA with lattice energy fluctuations is controlled by low lattice energy regions along the source length. Longer source lengths sample more of the varying lattice energy surface, so there are more opportunities for a dislocation to bow-out into a weak area, thus making FR source activation easier. The difference in size effect between the MPEA and the homogeneous material results in an increasing gap between their critical stresses. The MPEA sources become much weaker than the homogeneous material sources. For the 20b sources with the largest correlation length ($20w_0$) and variance, 33% of the sources in the distribution exceed the source strength of the homogeneous case. However, for the 60 sources for the same $l = 20w_0$ and for which the variance is the largest, just 12% of the sources exceed the homogeneous case. This trend implies that the longer FR sources in an MPEA are unlikely to exceed the strength of the homogeneous case due to the prevalence of low-strength areas.

The change in FR source activation mechanism with an MPEA also explains why the statistical variation in critical stresses

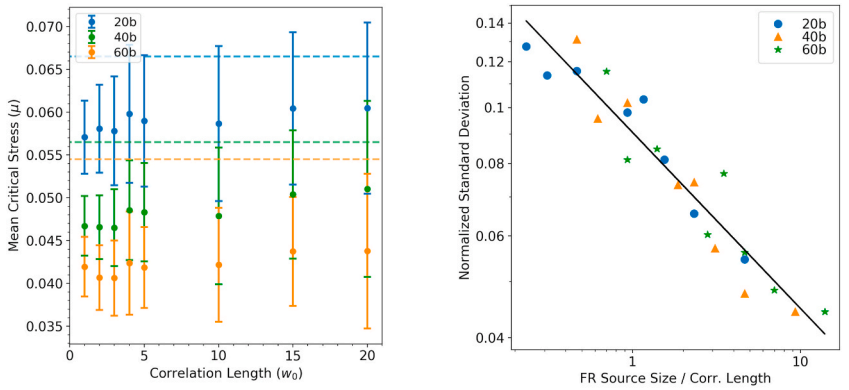

(a) Mean Critical Stress (b) Normalized Standard Deviation

Fig. 13. (a) The critical stresses for Frank-Read source activation at each l for three different Frank-Read source sizes. All calculations use a screw-oriented source and include the orientation-dependent resistance. In (a), the error bars represent the standard deviation of the critical stresses at each l. (b) The standard deviation of the critical stresses plotted against the ratio of source size to correlation length. The standard deviation is normalized by the average lattice energy coefficient, μ_{usf}/d_{110}. The linear relationship in the log-log plot reveals a power law relationship with an exponent of −0.30.

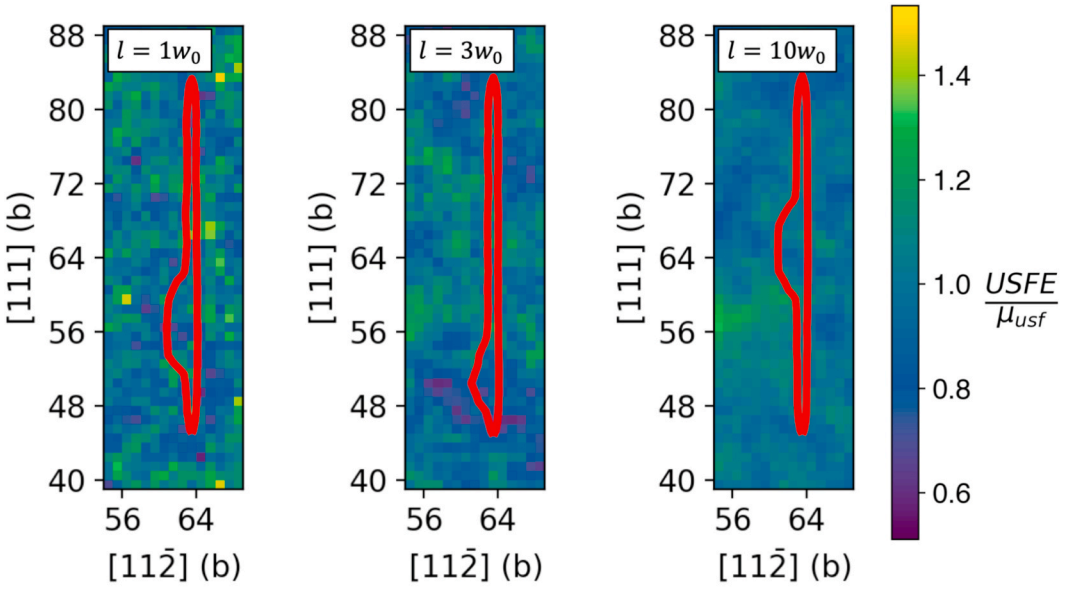

(a) 40b FR Source

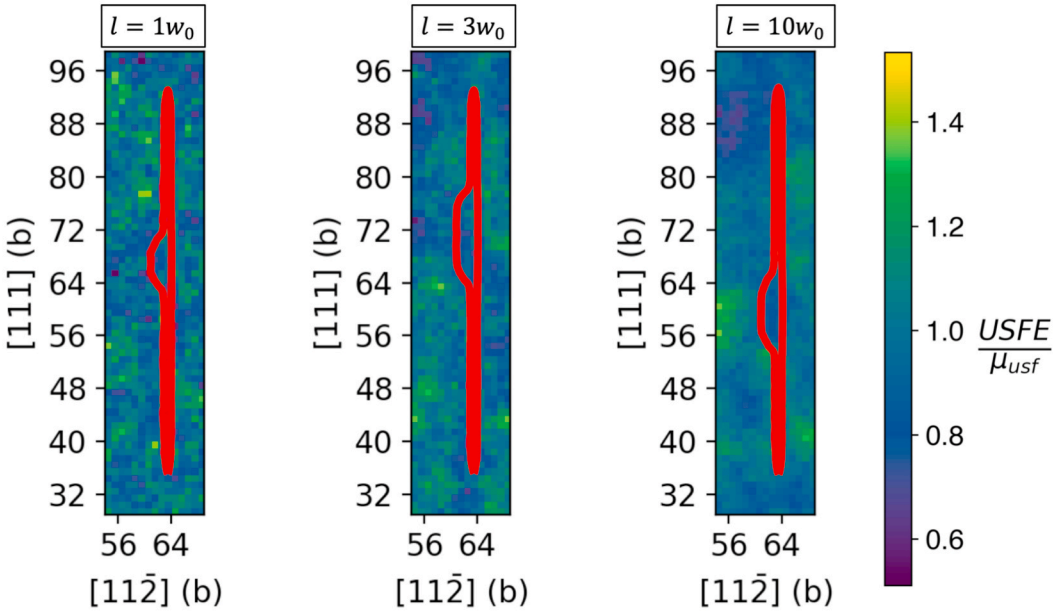

(b) 60b FR Source

Fig. 14. The initial stages of Frank-Read source activation for the larger 40 and 60 FR source lengths.

decreases with FR length L. Fig. 13b shows the standard deviation normalized by the mean lattice energy (μ_{usf}/d_{110}) for the three source sizes studied. When the results are plotted against the ratio of FR source size to l, the data points for all three source sizes collapse into a single curve. The source size to correlation length ratio can be thought of as a proxy for the number of peaks and valleys the FR source sees along its length. A higher ratio causes less variation in the critical stresses because the FR source is sampling a larger number of fluctuations within the slip plane, while sources with a low ratio are only sampling a few peaks and valleys and are thus much more dependent on the specific placement of the FR source. The magnitude of the standard deviation appears to be captured by

the number of peaks/valleys encountered by the source only, which suggests that the underlying variation in the lattice energy, which does not change with source size, is driving the variation of critical stresses. In fact, the standard deviation of the critical stresses follows a power-law relationship as the standard deviation scales with $(L/l)^{-0.30}$ as determined by the slope of the best-fit line in Fig. 13b.

5.3. Impact of the character-dependent energy barrier

To understand the effect of the character-dependent lattice energy barrier (Eq. (9)), several simulations were run with varying screw-edge ratios. The screw-edge ratio is calculated using MS, which requires classical potentials for the MPEA of interest. Since these potentials may not exist for multi-component systems or may not accurately capture dislocation behavior, it is important to understand the sensitivity of the PFDD calculations to these input parameters. As an extreme case, 24 of the Frank-Read sources (3 of each correlation length) were rerun using a screw-edge ratio of 30. Screw-edge ratios in pure BCC metals may be on the order of 10s–100s, but it is expected that the ratios in BCC MPEAs are much lower. With this extreme difference between screw and edge lattice energies, the maximum decrease in critical stress for screw-oriented sources is 0.02 μ. The average decrease in critical stress is 0.0098 μ, which is a 16.8% decrease relative to the original calculations with a screw-edge ratio of 4.65. The edge-oriented sources show an even smaller dependence on the screw-edge ratio, with an average critical stress decrease of 0.001 μ, a 3% decrease. Therefore, we conclude that the screw-edge ratio in PFDD has a higher order effect on the resulting critical stress compared to the underlying lattice energy fluctuations, which drive the statistical variation in critical stresses.

This work uses a simple, smooth interpolation between screw and edge energies for the character-dependent barrier (Eq. (9)), but other functional forms are possible. Peng et al. used a piecewise function with multiple local minimums for the character-dependent barrier of Nb and Ta, based on MS simulations of Ta (Peng et al., 2020). Such calculations of a wide range of dislocation character types are computationally intensive and heavily dependent on the chosen potential, so this type of data is rare even for pure metals, and does not currently exist for multi-component systems. Nevertheless, to compare the effect of the functional form of the character-dependence, we calculate the critical stress for a Frank-Read source in Nb using the character-dependence calculated for Ta (Kang et al., 2012). The Peierls stress has a local maximum at 71°, so dislocations of this character will be resistant to glide in addition to the pure screw dislocations. When the smoothly interpolated barrier is used (Eq. (9)), the critical stress drops from 0.0785 μ_{Nb} to 0.0435 μ_{Nb} for a screw-oriented source. However, when the Ta character-dependence is used, the critical stress does not change from the no character-dependence case. We attribute this to the immobile 71° dislocations which inhibits kink-pair migration. For the edge-oriented source, the critical stress increases slightly from 0.0295 μ_{Nb} for the smoothly interpolated barrier to 0.0345 μ_{Nb} for the Ta barrier. This is expected as the barrier function is 0.033 and 0.097 for edge dislocation with the smoothly interpolated barrier and Ta barrier, respectively. We conclude that the form of the barrier function does indeed affect the critical stress by either allowing or suppressing kink-pair migration.

5.4. Implications on plastic behavior

In this work, we considered glide on the $\{110\}\langle 111\rangle$ slip family, while in BCC crystals, slip on other families are possible. The present model can be used to study other slip modes and aid in identifying preferred systems (Xu et al., 2020c). Other modes will, however, have their own individual variations in energetic barriers and line orientation-dependencies, which would need to be taken into account. In principle, this methodology can also be used to study other refractory MPEAs, which will have their own distributions of local slip resistances and unique screw/edge differences (Xu et al., 2020a). Based on the present findings, it can be anticipated that MPEAs demonstrating greater fluctuations in composition or greater screw/edge mobility ratios would experience greater drops in the average FR critical stress drops relative to a homogeneous reference material. Moreover, since we have shown that the statistical dispersion in the critical stresses scales with that of the underlying variation in lattice energy, it can be expected that MPEAs with less variation in lattice energies among the short-ranged ordered compositions, the less variation in activation stresses and vice versa. Here, we did not directly address short-range ordering but generally, our findings imply that the range of chemical ordering, represented here by higher values of l, affects the statistical variation in the critical stresses for activating sources and less so the mean value.

The statistical distribution of critical stresses for FR sources in the material can have macroscopic effects on its stress-strain behavior. Weaker FR sources will be activated quickly, which may lead to a high dislocation density and increased work hardening. Additionally, as the stress is increased, stronger FR sources will be activated, increasing the work hardening even further. Recent work on nanocrystalline metals, in which double-pinned sources in grain boundaries are the primary source for dislocations, find that with more variation in source strengths, the greater the strain hardening rate (Yuan et al., 2015, 2016).

While not explicitly considered here, as a dislocation slips through a crystal, the local compositions will change, which will alter the local USFE for subsequent dislocations (Xu et al., 2020a; Li et al., 2019a). Hence, we can predict that after an FR source emits one dislocation loop at its critical stress, the underlying lattice energy surface will change, and a new critical stress for that FR source will be drawn from the lognormal distributions we have calculated. This may lead to FR sources with low critical stresses being exhausted quickly, leaving behind a predominance of strong FR sources.

6. Conclusions

In conclusion, we have extended the phase field dislocation dynamics (PFDD) formulation to study refractory multi-principal element alloys (MPEAs) by including a spatially varying lattice energy coefficient and a dislocation character-dependence in the

lattice energy. We use this new formulation to study the behavior of Frank-Read (FR) sources in MoNbTi. We observe that the shape of the dislocation loop depends on the underlying correlation length, *l*, of the MPEA and the orientation of the FR source. The average critical stress to activate the FR source and create a full dislocation loop is not influenced by the underlying *l*, but the variance in the critical stress does increase with clustering, represented by higher *l*. We also find the critical stress for an FR source in the MPEA is on average lower than in the homogeneous MoNbTi due to a shift in mechanism for creating the initial dislocation bow-out. In the MPEA, the dislocation is able to create an athermal kink-pair into a lower energy region first and then expand outwards, allowing the dislocation loop to grow at a lower stress. This shift in mechanism leads to a significant size effect as the critical stress is dependent on the sampling of the underlying lattice energy surface, instead of merely the line tension of the dislocation bow-out. The statistical nature of FR sources in refractory MPEAs may play a role in their macroscopic mechanical properties by increasing dislocation densities and strain hardening.

Author contribution

Lauren Smith: Conceptualization, Methodology, Software, Visualization, Writing – Original Draft.
Yanqing Su: Methodology, Investigation, Writing – Original Draft.
Shuozhi Xu: Methodology, Software, Investigation, Writing – Original Draft.
Abigail Hunter: Conceptualization, Supervision, Writing – Review and Editing.
Irene Beyerlein: Conceptualization, Supervision, Project Administration, Writing – Review and Editing.

Declaration of competing interest

The authors declare that they have no known competing financial interests or personal relationships that could have appeared to influence the work reported in this paper.

Acknowledgements

LS acknowledges support from the Department of Energy National Nuclear Security Administration Stewardship Science Graduate Fellowship, which is provided under cooperative agreement number DE-NA0003960. The work of SX was supported in part by the Elings Prize Fellowship in Science offered by the California NanoSystems Institute (CNSI) on the UC Santa Barbara campus. LS, YS, SX, and IJB gratefully acknowledge support from the Office of Naval Research under contract ONR BRC Grant N00014-18-1-2392. Use was made of computational facilities purchased with funds from the National Science Foundation (CNS-1725797) and administered by the Center for Scientific Computing (CSC). The CSC is supported by the CNSI and the Materials Research Science and Engineering Center (MRSEC; NSF DMR 1720256) at UC Santa Barbara. AH gratefully acknowledges support from support from the Materials project within the Physics and Engineering Models (PEM) Subprogram element of the Advanced Simulation and Computing (ASC) Program at Los Alamos National Laboratory (LANL).

References

Albrecht, C., Hunter, A., Kumar, A., Beyerlein, I.J., 2020. A phase field model for dislocations in hexagonal close packed crystals. J. Mech. Phys. Solid. 137, 103823. https://doi.org/10.1016/j.jmps.2019.103823.

Bahramyan, M., Mousavian, R.T., Brabazon, D., 2020. Study of the plastic deformation mechanism of TRIP-TWIP high entropy alloys at the atomic level. Int. J. Plast. 127, 102649. https://doi.org/10.1016/j.ijplas.2019.102649.

Beyerlein, I.J., Hunter, A., 2016. Understanding nanoscale dislocation mechanics using phase field dislocation dynamics. Philos. Trans. R. Soc. A 374, 20150166. https://doi.org/10.1098/rsta.2015.0166.

Brechtl, J., Chen, S.Y., Xie, X., Ren, Y., Qiao, J.W., Liaw, P.K., Zinkle, S.J., 2019. Towards a greater understanding of serrated flows in an Al-containing high-entropy-based alloy. Int. J. Plast. 115, 71–92. https://doi.org/10.1016/j.ijplas.2018.11.011.

Chaussidon, J., Fivel, M., Rodney, D., 2006. The glide of screw dislocations in bcc Fe: atomistic static and dynamic simulations. Acta Mater. 54, 3407–3416. https://doi.org/10.1016/j.actamat.2006.03.044.

Chen, B., Li, S., Zong, H., Ding, X., Sun, J., Ma, E., 2020a. Unusual activated processes controlling dislocation motion in body-centered-cubic high-entropy alloys. Proc. Natl. Acad. Sci. Unit. States Am. 117, 16199–16206. https://doi.org/10.1073/pnas.1919136117.

Chen, T., Yuan, R., Beyerlein, I.J., Zhou, C., 2020b. Predicting the size scaling in strength of nanolayered materials by a discrete slip crystal plasticity model. Int. J. Plast. 124, 247–260. https://doi.org/10.1016/j.ijplas.2019.08.016.

Choi, W.M., Jo, Y.H., Sohn, S.S., Lee, S., Lee, B.J., 2018. Understanding the physical metallurgy of the CoCrFeMnNi high-entropy alloy: an atomistic simulation study. NPJ Comput. Mater. 4, 1. https://doi.org/10.1038/s41524-017-0060-9, 10.1038/s41524-017-0060-9.

Couzinié, J.P., Dirras, G., 2018. Body-centered cubic high-entropy alloys: from processing to underlying deformation mechanisms. Mater. Char. 147, 533–544. https://doi.org/10.1016/J.MATCHAR.2018.07.015.

Couzinié, J.P., Lilensten, L., Champion, Y., Dirras, G., Perrière, L., Guillot, I., 2015. On the room temperature deformation mechanisms of a TiZrHfNbTa refractory high-entropy alloy. Mater. Sci. Eng., A 645, 255–263. https://doi.org/10.1016/j.msea.2015.08.024.

Dezerald, L., Proville, L., Ventelon, L., Willaime, F., Rodney, D., 2015. First-principle prediction of kink-pair activation enthalpy on screw dislocations in bcc transition metals: V, Nb, Ta, Mo, W, and Fe. Phys. Rev. B 91, 094105. https://doi.org/10.1103/PhysRevB.91.094105.

Dezerald, L., Ventelon, L., Clouet, E., Denoual, C., Rodney, D., Willaime, F., 2014. Ab initio modeling of the two-dimensional energy landscape of screw dislocations in bcc transition metals. Phys. Rev. B 89, 1–13. https://doi.org/10.1103/PhysRevB.89.024104.

Ding, J., Yu, Q., Asta, M., Ritchie, R.O., 2018. Tunable stacking fault energies by tailoring local chemical order in crconi medium-entropy alloys. Proc. Natl. Acad. Sci. Unit. States Am. 115, 8919–8924. https://doi.org/10.1073/pnas.1808660115.

Dirras, G., Gubicza, J., Heczel, A., Lilensten, L., Couzinié, J.P., Perrière, L., Guillot, I., Hocini, A., 2015. Microstructural investigation of plastically deformed $Ti_{20}Zr_{20}Hf_{20}Nb_{20}Ta_{20}$ high entropy alloy by X-ray diffraction and transmission electron microscopy. Mater. Char. 108, 1–7. https://doi.org/10.1016/j.matchar.2015.08.007.

El Ters, P., Shehadeh, M.A., 2019. Modeling the temperature and high strain rate sensitivity in bcc iron: atomistically informed multiscale dislocation dynamics simulations. Int. J. Plast. 112, 257–277. https://doi.org/10.1016/j.ijplas.2018.09.002.
Fernández-Caballero, A., Wróbel, J.S., Mummery, P.M., Nguyen-Manh, D., 2017. Short-range order in high entropy alloys: theoretical formulation and application to Mo-Nb-Ta-V-W system. J. Phase Equilibria Diffus. 38, 391–403. https://doi.org/10.1007/s11669-017-0582-3 arXiv:1705.01844.
Foreman, A.J., 1967. The bowing of a dislocation segment. Philos. Mag. A 15, 1011–1021. https://doi.org/10.1080/14786436708221645.
Frank, F.C., Read, W.T., 1950. Multiplication processes for slow moving dislocations. Phys. Rev. 79, 722–723. https://doi.org/10.1103/PhysRev.79.722.
Gali, A., George, E., 2013. Tensile properties of high- and medium-entropy alloys. Intermetallics 39, 74–78. https://doi.org/10.1016/j.intermet.2013.03.018.
Gröger, R., Vitek, V., 2020. Single crystal yield criterion for chromium based on atomistic studies of isolated 1/2[111] screw dislocations. Int. J. Plast. 102733doi. https://doi.org/10.1016/j.ijplas.2020.102733.
Hale, L.M., Zimmerman, J.A., Weinberger, C.R., 2014. Simulations of bcc tantalum screw dislocations: why classical inter-atomic potentials predict 112 slip. Comput. Mater. Sci. 90, 106–115. https://doi.org/10.1016/j.commatsci.2014.03.064.
Hasan, M., Liu, Y., An, X., Gu, J., Song, M., Cao, Y., Li, Y., Zhu, Y., Liao, X., 2019. Simultaneously enhancing strength and ductility of a high-entropy alloy via gradient hierarchical microstructures. Int. J. Plast. 123, 178–195. https://doi.org/10.1016/j.ijplas.2019.07.017.
Hu, Y.Z., Tonder, K., 1992. Simulation of 3-D random rough surface by 2-D digital filter and fourier analysis. Int. J. Mach. Tool Manufact. https://doi.org/10.1016/0890-6955(92)90064-N.
Hunter, A., Beyerlein, I.J., 2015. Relationship between monolayer stacking faults and twins in nanocrystals. Acta Mater. 88, 207–217. https://doi.org/10.1016/j.actamat.2014.12.045.
Ismail-Beigi, S., Arias, T.A., 2000. *Ab initio* study of screw dislocations in Mo and Ta: a new picture of plasticity in bcc transition metals. Phys. Rev. Lett. 84, 1499–1502. https://doi.org/10.1103/PhysRevLett.84.1499 arXiv:9908110.
Itakura, M., Kaburaki, H., Yamaguchi, M., 2012. First-principles study on the mobility of screw dislocations in bcc iron. Acta Mater. 60, 3698–3710. https://doi.org/10.1016/j.actamat.2012.03.033.
Ji, R., Phan, T., Chen, H., Xiong, L., 2020. Quantifying the dynamics of dislocation kinks in iron and tungsten through atomistic simulations. Int. J. Plast. 128, 102675. https://doi.org/10.1016/j.ijplas.2020.102675.
Kang, K., Bulatov, V.V., Cai, W., 2012. Singular orientations and faceted motion of dislocations in body-centered cubic crystals. Proc. Natl. Acad. Sci. Unit. States Am. 109, 15174–15178. https://doi.org/10.1073/pnas.1206079109.
Koslowski, M., Cuitiño, A.M., Ortiz, M., 2002. A phase-field theory of dislocation dynamics, strain hardening and hysteresis in ductile single crystals. J. Mech. Phys. Solid. 50, 2597–2635. https://doi.org/10.1016/S0022-5096(02)00037-6 arXiv:0109447.
Kröner, E., 1959. Allgemeine kontinuumstheorie der versetzungen und eigenspannungen. Arch. Ration. Mech. Anal. 4, 273.
Li, Q.J., Sheng, H., Ma, E., 2019a. Strengthening in multi-principal element alloys with local-chemical-order roughened dislocation pathways. Nat. Commun. 10, 1–11. https://doi.org/10.1038/s41467-019-11464-7 arXiv:1904.07681.
Li, X.G., Chen, C., Zheng, H., Zuo, Y., Ong, S.P., 2020. Complex strengthening mechanisms in the NbMoTaW multi-principal element alloy. NPJ Comput. Mater. 6, 1–10. https://doi.org/10.1038/s41524-020-0339-0.
Li, Z., Zhao, S., Ritchie, R.O., Meyers, M.A., 2019b. Mechanical properties of high-entropy alloys with emphasis on face-centered cubic alloys. Prog. Mater. Sci. 102, 296–345. https://doi.org/10.1016/j.pmatsci.2018.12.003.
Lilensten, L., Couzinié, J.P.P., Perrière, L., Hocini, A., Keller, C., Dirras, G., Guillot, I., 2018. Study of a bcc multi-principal element alloy: tensile and simple shear properties and underlying deformation mechanisms. Acta Mater. 142, 131–141. https://doi.org/10.1016/j.actamat.2017.09.062.
Mapar, A., Ghassemi-Armaki, H., Pourboghrat, F., Kumar, K.S., 2017. A differential-exponential hardening law for non-schmid crystal plasticity finite element modeling of ferrite single crystals. Int. J. Plast. 91, 268–299. https://doi.org/10.1016/j.ijplas.2016.11.009.
Maresca, F., Curtin, W.A., 2020a. Mechanistic origin of high strength in refractory BCC high entropy alloys up to 1900K. Acta Mater. 182, 235–249. https://doi.org/10.1016/j.actamat.2019.10.015 arXiv:1901.02100.
Maresca, F., Curtin, W.A., 2020b. Theory of screw dislocation strengthening in random BCC alloys from dilute to “High-Entropy” alloys. Acta Mater. 182, 144–162. https://doi.org/10.1016/j.actamat.2019.10.007.
Ming, K., Bi, X., Wang, J., 2019. Strength and ductility of CrFeCoNiMo alloy with hierarchical microstructures. Int. J. Plast. 113, 255–268. https://doi.org/10.1016/j.ijplas.2018.10.005.
Miracle, D.B., Senkov, O.N., 2017. A critical review of high entropy alloys and related concepts. Acta Mater. 122, 448–511. https://doi.org/10.1016/j.actamat.2016.08.081.
Mompiou, F., Tingaud, D., Chang, Y., Gault, B., Dirras, G., 2018. Conventional vs harmonic-structured β-Ti-25Nb-25Zr alloys: a comparative study of deformation mechanisms. Acta Mater. 161, 420–430. https://doi.org/10.1016/j.actamat.2018.09.032.
Otto, F., Dlouhy, A., Somsen, C., Bei, H., Eggeler, G., George, E., 2013. The influences of temperature and microstructure on the tensile properties of a cocrfemnni high-entropy alloy. Acta Mater. 61, 5743–5755. https://doi.org/10.1016/j.actamat.2013.06.018.
Peng, X., Mathew, N., Beyerlein, I.J., Dayal, K., Hunter, A., 2020. A 3D phase field dislocation dynamics model for body-centered cubic crystals. Comput. Mater. Sci. 171, 109217. https://doi.org/10.1016/j.commatsci.2019.109217.
Rao, S., Varvenne, C., Woodward, C., Parthasarathy, T., Miracle, D., Senkov, O., Curtin, W., 2017a. Atomistic simulations of dislocations in a model BCC multicomponent concentrated solid solution alloy. Acta Mater. 125, 311–320. https://doi.org/10.1016/J.ACTAMAT.2016.12.011.
Rao, S.I., Akdim, B., Antillon, E., Woodward, C., Parthasarathy, T.A., Senkov, O.N., 2019a. Modeling solution hardening in BCC refractory complex concentrated alloys: NbTiZr, $Nb_{1.5}TiZr_{0.5}$ and $Nb_{0.5}TiZr_{1.5}$. Acta Mater. 168, 222–236. https://doi.org/10.1016/j.actamat.2019.02.013.
Rao, S.I., Antillon, E., Woodward, C., Akdim, B., Parthasarathy, T.A., Senkov, O.N., 2019b. Solution hardening in body-centered cubic quaternary alloys interpreted using Suzuki’s kink-solute interaction model. Scripta Mater. 165, 103–106. https://doi.org/10.1016/j.scriptamat.2019.02.012.
Rao, S.I., Woodward, C., Parthasarathy, T.A., Senkov, O., 2017b. Atomistic simulations of dislocation behavior in a model FCC multicomponent concentrated solid solution alloy. Acta Mater. 134, 188–194. https://doi.org/10.1016/j.actamat.2017.05.071.
Schneider, M., George, E.P., Manescau, T.J., Záležák, T., Hunfeld, J., Dlouhý, A., Eggeler, G., Laplanche, G., 2020. Analysis of strengthening due to grain boundaries and annealing twin boundaries in the CrCoNi medium-entropy alloy. Int. J. Plast. 124, 155–169. https://doi.org/10.1016/j.ijplas.2019.08.009.
Seeger, A., 1956. On the theory of the low-temperature internal friction peak observed in metals. Phil. Mag. 1, 651–662. https://doi.org/10.1080/14786435608244000.
Senkov, O.N., Miracle, D.B., Chaput, K.J., Couzinie, J.P., 2018. Development and exploration of refractory high entropy alloys — a review. J. Mater. Res. 33, 3092–3128. https://doi.org/10.1557/jmr.2018.153.
Senkov, O.N., Rao, S.I., Butler, T.M., Chaput, K.J., 2019. Ductile Nb alloys with reduced density and cost. J. Alloys Compd. 808, 151685. https://doi.org/10.1016/j.jallcom.2019.151685.
Shinzato, S., Wakeda, M., Ogata, S., 2019. An atomistically informed kinetic Monte Carlo model for predicting solid solution strengthening of body-centered cubic alloys. Int. J. Plast. 122, 319–337. https://doi.org/10.1016/j.ijplas.2019.03.004.
Singh, P., Smirnov, A.V., Johnson, D.D., 2015. Atomic short-range order and incipient long-range order in high-entropy alloys. Phys. Rev. B 91, 224204, 10.1103/PhysRevB.91.224204. https://link.aps.org/doi/10.1103/PhysRevB.91.224204.
Statham, C.D., Koss, D.A., Christian, J.W., 1972. The thermally activated deformation of niobium-molybdenum and niobium-rhenium alloy single crystals. Philos. Mag. A 26, 1089–1103. https://doi.org/10.1080/14786437208227366.
Su, Y., Ardeljan, M., Knezevic, M., Jain, M., Pathak, S., Beyerlein, I.J., 2020. Elastic constants of pure body-centered cubic Mg in nanolaminates. Comput. Mater. Sci. 174, 109501, 10.1016/j.commatsci.2019.109501. http://www.sciencedirect.com/science/article/pii/S0927025619308006.
Su, Y., Xu, S., Beyerlein, I.J., 2019a. Density functional theory calculations of generalized stacking fault energy surfaces for eight face-centered cubic transition metals. J. Appl. Phys. 126, 105112, 10.1063/1.5115282. https://aip.scitation.org/doi/10.1063/1.5115282.

Su, Y., Xu, S., Beyerlein, I.J., 2019b. *Ab initio*-informed phase-field modeling of dislocation core structures in equal-molar CoNiRu multi-principal element alloys. Model. Simulat. Mater. Sci. Eng. 27, 084001 https://doi.org/10.1088/1361-651x/ab3b62.

Ventelon, L., Willaime, F., Clouet, E., Rodney, D., 2013. Ab initio investigation of the Peierls potential of screw dislocations in bcc Fe and W. Acta Mater. 61, 3973–3985. https://doi.org/10.1016/j.actamat.2013.03.012.

Wang, F., Balbus, G.H., Xu, S., Su, Y., Shin, J., Rottmann, P.F., Knipling, K.E., Stinville, J.C., Mills, L.H., Senkov, O.N., Beyerlein, I.J., Pollock, T.M., Gianola, D.S., 2020. Multiplicity of dislocation pathways in a refractory multi-principal element alloy. Science.

Weinberger, C.R., Boyce, B.L., Battaile, C.C., 2013a. Slip planes in bcc transition metals. Int. Mater. Rev. 58, 296–314. https://doi.org/10.1179/1743280412Y.0000000015.

Weinberger, C.R., Tucker, G.J., Foiles, S.M., 2013b. Peierls potential of screw dislocations in bcc transition metals: predictions from density functional theory. Phys. Rev. B 87, 1–8. https://doi.org/10.1103/PhysRevB.87.054114.

Wróbel, J.S., Nguyen-Manh, D., Lavrentiev, M.Y., Muzyk, M., Dudarev, S.L., 2015. Phase stability of ternary fcc and bcc fe-cr-ni alloys. Phys. Rev. B 91, 024108, 10.1103/PhysRevB.91.024108. https://link.aps.org/doi/10.1103/PhysRevB.91.024108.

Xu, S., Hwang, E., Jian, W.R., Su, Y., Beyerlein, I.J., 2020a. Atomistic calculations of the generalized stacking fault energies in two refractory multi-principal element alloys. Intermetallics 124, 106844. https://doi.org/10.1016/j.intermet.2020.106844.

Xu, S., Mianroodi, J.R., Hunter, A., Beyerlein, I.J., Svendsen, B., 2019a. Phase-field-based calculations of the disregistry fields of static extended dislocations in FCC metals. Philos. Mag. A 99, 1400–1428. https://doi.org/10.1080/14786435.2019.1582850.

Xu, S., Mianroodi, J.R., Hunter, A., Svendsen, B., Beyerlein, I.J., 2020b. Comparative modeling of the disregistry and Peierls stress for dissociated edge and screw dislocations in Al. Int. J. Plast. 129, 102689. https://doi.org/10.1016/j.ijplas.2020.102689.

Xu, S., Smith, L., Mianroodi, J.R., Hunter, A., Svendsen, B., Beyerlein, I.J., 2019b. A comparison of different continuum approaches in modeling mixed-type dislocations in Al. Model. Simulat. Mater. Sci. Eng. 27, 074004 https://doi.org/10.1088/1361-651X/ab2d16.

Xu, S., Su, Y., Beyerlein, I.J., 2019c. Modeling dislocations with arbitrary character angle in face-centered cubic transition metals using the phase-field dislocation dynamics method with full anisotropic elasticity. Mech. Mater. 139, 103200. https://doi.org/10.1016/j.mechmat.2019.103200.

Xu, S., Su, Y., Smith, L.T.W., Beyerlein, I.J., 2020c. Frank-Read source operation in six body-centered cubic refractory metals. J. Mech. Phys. Solid. 141, 104017. https://doi.org/10.1016/j.jmps.2020.104017.

Yuan, R., Beyerlein, I.J., Zhou, C., 2015. Emergence of grain-size effects in nanocrystalline metals from statistical activation of discrete dislocation sources. Acta Mater. 90, 169–181. https://doi.org/10.1016/j.actamat.2015.02.035.

Yuan, R., Beyerlein, I.J., Zhou, C., 2016. Coupled crystal orientation-size effects on the strength of nano crystals. Sci. Rep. 6, 26254. https://doi.org/10.1038/srep26254.

Zeng, Y., Cai, X., Koslowski, M., 2019. Effects of the stacking fault energy fluctuations on the strengthening of alloys. Acta Mater. 164, 1–11. https://doi.org/10.1016/j.actamat.2018.09.066.

Zhai, J.H., Zaiser, M., 2019. Properties of dislocation lines in crystals with strong atomic-scale disorder. Mater. Sci. Eng., A 740–741, 285–294. https://doi.org/10.1016/j.msea.2018.10.010.

Zhang, F.X., Zhao, S., Jin, K., Xue, H., Velisa, G., Bei, H., Huang, R., Ko, J.Y.P., Pagan, D.C., Neuefeind, J.C., Weber, W.J., Zhang, Y., 2017. Local structure and short-range order in a nicocr solid solution alloy. Phys. Rev. Lett. 118, 205501, 10.1103/PhysRevLett.118.205501. https://link.aps.org/doi/10.1103/PhysRevLett.118.205501.

Zhang, L., Xiang, Y., Han, J., Srolovitz, D.J., 2019. The effect of randomness on the strength of high-entropy alloys. Acta Mater. 166, 424–434. https://doi.org/10.1016/j.actamat.2018.12.032.

Zhang, R., Zhao, S., Ding, J., Chong, Y., Jia, T., Ophus, C., Asta, M., Ritchie, R.O., Minor, A.M., 2020. Short-range order and its impact on the CrCoNi medium-entropy alloy. Nature 581, 283–287. https://doi.org/10.1038/s41586-020-2275-z, 10.1038/s41586-020-2275-z.

Zhang, Y., Ngan, A.H.W., 2018. Dislocation-density dynamics for modeling the cores and peierls stress of curved dislocations. Int. J. Plast. 104, 1–22. https://doi.org/10.1016/j.ijplas.2018.01.009.

Zhang, Y., Zuo, T.T., Tang, Z., Gao, M.C., Dahmen, K.A., Liaw, P.K., Lu, Z.P., 2014. Microstructures and properties of high-entropy alloys. Prog. Mater. Sci. 61, 1–93. https://doi.org/10.1016/j.pmatsci.2013.10.001.

Zhao, S., Osetsky, Y., Stocks, M., Zhang, Y., 2019. Local-environment dependence of stacking fault energies in concentrated solid-solution alloys. NPJ Comput. Mater. 5 https://doi.org/10.1038/s41524-019-0150-y.

Zhu, Y., Wang, H., Zhu, X., Xiang, Y., 2014. A continuum model for dislocation dynamics incorporating frank-read sources and hall-petch relation in two dimensions. Int. J. Plast. 60, 19–39. https://doi.org/10.1016/j.ijplas.2014.04.013.